AFRL-RV-PS-
TR-2019-0159

EFFECT OF THE EXPLOSIVE TYPE ON ROCK DAMAGE/FRACTURING AND SEISMIC RADIATION

Anastasia Stroujkova, et al.

Applied Research Associates
Weston Geophysical Group
181 Bedford Street, Suite 1
Lexington, MA 02420

August 28, 2019

Final Report

AIR FORCE RESEARCH LABORATORY
Space Vehicles Directorate
3550 Aberdeen Ave SE
AIR FORCE MATERIEL COMMAND
KIRTLAND AIR FORCE BASE, NM 87117-5776

DTIC COPY

NOTICE AND SIGNATURE PAGE

AFRL-RV-PS-TR-2019-0159 HAS BEEN REVIEWED AND IS APPROVED FOR PUBLICATION IN ACCORDANCE WITH ASSIGNED DISTRIBUTION STATEMENT.

//SIGNED//	//SIGNED//
Dr. Frederick Schult	Dr. Thomas R. Caudill, Chief
Program Manager, AFRL/RVB	AFRL Geospace Technologies Division

REPORT DOCUMENTATION PAGE

Form Approved
OMB No. 0704-0188

1. REPORT DATE *(DD-MM-YYYY)*	**2. REPORT TYPE**	**3. DATES COVERED** *(From - To)*
28-08-2019	Final Report	08 Aug 2018 – 16 Aug 2019

4. TITLE AND SUBTITLE
Effect of the Explosive Type on Rock Damage/Fracturing and Seismic Radiation

5a. CONTRACT NUMBER
FA9453-18-C-0060

5b. GRANT NUMBER

5c. PROGRAM ELEMENT NUMBER
62601F

6. AUTHOR(S)
Anastasia Stroujkova, Mark Leidig, Vanessa Napoli, Peter Hubbard, Jeremy Salerno, and James Lewkowicz

5d. PROJECT NUMBER
1010

5e. TASK NUMBER
EF133292

5f. WORK UNIT NUMBER
V1HW

7. PERFORMING ORGANIZATION NAME(S) AND ADDRESS(ES)
Applied Research Associates
Weston Geophysical Group
181 Bedford Street, Suite 1
Lexington, MA 02420

8. PERFORMING ORGANIZATION REPORT NUMBER

9. SPONSORING / MONITORING AGENCY NAME(S) AND ADDRESS(ES)
Air Force Research Laboratory
Space Vehicles Directorate
3550 Aberdeen Avenue SE
Kirtland AFB, NM 87117-5776

10. SPONSOR/MONITOR'S ACRONYM(S)
AFRL/RVBN

11. SPONSOR/MONITOR'S REPORT NUMBER(S)
AFRL-RV-PS-TR-2019-0159

12. DISTRIBUTION / AVAILABILITY STATEMENT
Approved for public release; distribution is unlimited (AFMC-2019-0758 dtd 29 Nov 2019).

13. SUPPLEMENTARY NOTES

14. ABSTRACT
In 2016, we conducted a series of chemical explosions using aluminized and non-aluminized explosives in the same location to quantify the effects of the gaseous products on the radiated seismic energy. Even though the experiment produced important results, the data analysis posed additional questions including: (a) the individual effects of the velocity of detonation, chemistry, and the temperature of the gaseous products on the seismic amplitudes and spectra, (b) the effect of the oxygen balance of the explosives on their performance and the seismic wave amplitudes, and (c) the effect of the borehole and other man-made features on the non-isotropic seismic radiation. The current project is an extension of the previous experimental study (Contract No FA9453-16-C-0021) intended to isolate and quantify the effects of the individual explosive properties on seismic amplitudes and spectra. The new experiment included 4 additional explosions (two COMP B shots, one HBX-1 shot and one Octol shot) in hard rock. The combination of the explosives is designed to address the unresolved issues of explosion coupling and energy partitioning between the thermal and mechanical explosive components.

15. SUBJECT TERMS
explosion seismic source generation

16. SECURITY CLASSIFICATION OF:			**17. LIMITATION OF ABSTRACT**	**18. NUMBER OF PAGES**	**19a. NAME OF RESPONSIBLE PERSON**
a. REPORT	**b. ABSTRACT**	**c. THIS PAGE**			Dr. Frederick Schult
Unclassified	Unclassified	Unclassified	Unlimited	62	**19b. TELEPHONE NUMBER** *(include area code)*

This page is intentionally left blank.

TABLE OF CONTENTS

LIST OF FIGURES

LIST OF TABLES

1. SUMMARY

The current project is an extension of the previous experimental study (Contract No FA9453-16-C-0021) intended to isolate and quantify the effects of the individual explosive properties on seismic amplitudes and spectra. A previous experimental study (GAS2016; e.g. Stroujkova et al, 2018a) has shown that the fraction of energy radiated as seismic waves (or seismic efficiency) depends on the physical processes taking place at the source. It was also shown that the frequency spectra are affected by the explosive type. For instance, low-frequency *P*-wave amplitudes appear to be affected by the explosive velocity of detonation (VOD; Stroujkova, 2015a) and by the thermodynamic characteristics of gaseous explosive products (Stroujkova, 2015b). The GAS2016 experiment addressed the differences in the TNT and ANFO explosions conducted in both dry and water-filled boreholes. The experiment has shown that the explosives with slow VOD and high volume of the gas products not only generate higher amplitudes in the low-frequency part of the spectrum, but also result in higher azimuthal source anisotropy.

To further address the effect of the explosive type on seismic wave generation, we conducted additional explosions in the same quarry (GAS2018). The new explosion series included four explosions (two COMP B shots, one HBX-1 shot and one Octol shot) in hard rock. The explosives with higher VOD were used to address the unresolved issues of explosion coupling and energy partitioning between the thermal and mechanical explosive components. The current study combines the results of GAS2016 and GAS2018 to compare the explosives with a broad range of the VOD between 4200 m/s and 8450 m/s.

The major activity during this project was execution of the GAS2018 experiment. The major milestones of the work performed during this period include:

1. Experiment design is described in Chapter 2.
2. Seismic data acquisition, involving seismic network installation and data recording are discussed in Section 2.5 of this Report.
3. Drilling back into the shot boreholes and geophysical site characterization (well logging) is explained in Chapter 3 of the Report.
4. Analysis of the seismic waveforms, spectra and radiation patterns is provided in Chapter 4.
5. Yield estimate using both body and surface waves is given in Chapter 5.
6. Analysis of the acoustic waves is presented in Chapter 6.

The results of the study confirmed our earlier observations of seismic amplitude decrease with the increase in the VOD. The amplitude decrease is more pronounced for the low-frequency *P*-waves and for the surface waves. We observe a significant decrease in *Rg* amplitudes with respect to *P* amplitudes with the increase in the VOD, attributed to the increase in relative strength of the vertical dipole component of the moment tensor (parameter *K*, e.g. Patton and Taylor, 2008). For two of the explosions, the increase in the value of *K* coincides with a containment failure and crater formation corresponding to a more significant medium damage. These observations provide additional insight into the explosion source phenomenology.

2. GAS2018 EXPERIMENT

Anastasia Stroujkova, Mark Leidig, James Lewkowicz, Vanessa Napoli, Peter Hubbard, Jeremy Salerno

2.1. Introduction

Weston Geophysical Corp. (currently Weston Geophysical Group, Applied Research Associates) conducted a series of chemical explosions using various explosive types in order to investigate their effect on seismic signatures. The experiment was conducted in a granite quarry near the town of Carroll, NH (Fig. 1-2). The quarry is located within the Ordovician gneiss dome, which belongs to Oliverian Plutonic Suite (age 440 ± 40 Ma; Naylor, 1969; Lyons et al, 1997). The rocks of the formation are represented by foliated biotite gneiss with bands of amphibolite (Naylor, 1969; Bennett et al, 2006).

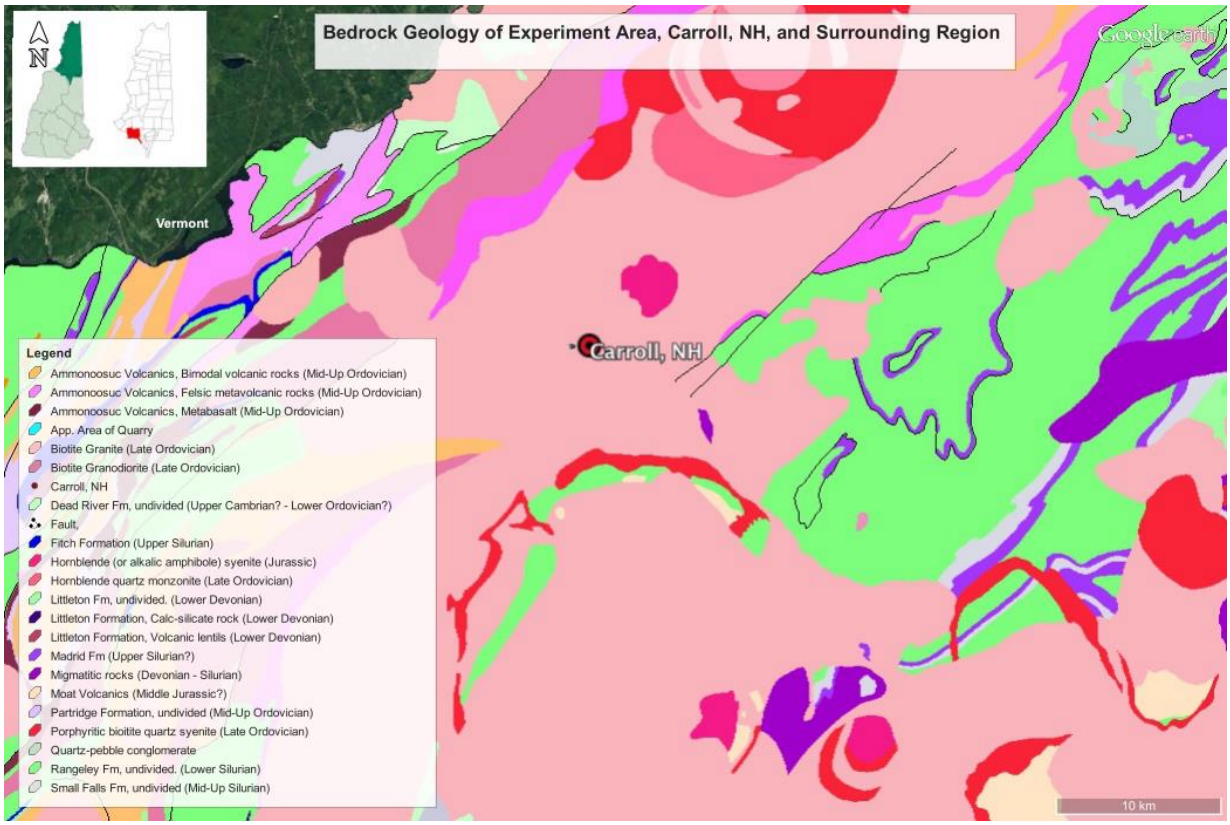

Figure 1. USGS New Hampshire bedrock lithology overlaid onto Google Earth satellite imagery. ***Carroll, NH and the experiment area (center, red circle) are shown within the Biotite granite (Late Ordovician).***

Four explosions were conducted in 2018, in addition to 6 explosions conducted in 2016. One of the explosions (SG1) was conducted in June, 2018 as a part of the separate Diffusion Experiment (designated as SD2 for the Diffusion Experiment, a project funded by the Defense Threat

Reduction Agency under Grant No. HDTRA1-17-1-0040). The remaining three explosions (SG2, SG3 and SG4) were detonated in October 2018. The map of the test site showing the locations of the shots is presented in Figure 2. The various explosions were detonated using different explosive types to study the effect of the explosive characteristics on the generated seismic waves. Shot SG1 was to be compared against SG2 (another COMP B shot in cemented borehole) and to Shot SG3 (HBX-1: RDX/TNT/Al/wax 40/38/17/5). The last explosion was detonated using Octol (HMX/TNT 75/25), which has the fastest VOD of all the explosions in the series.

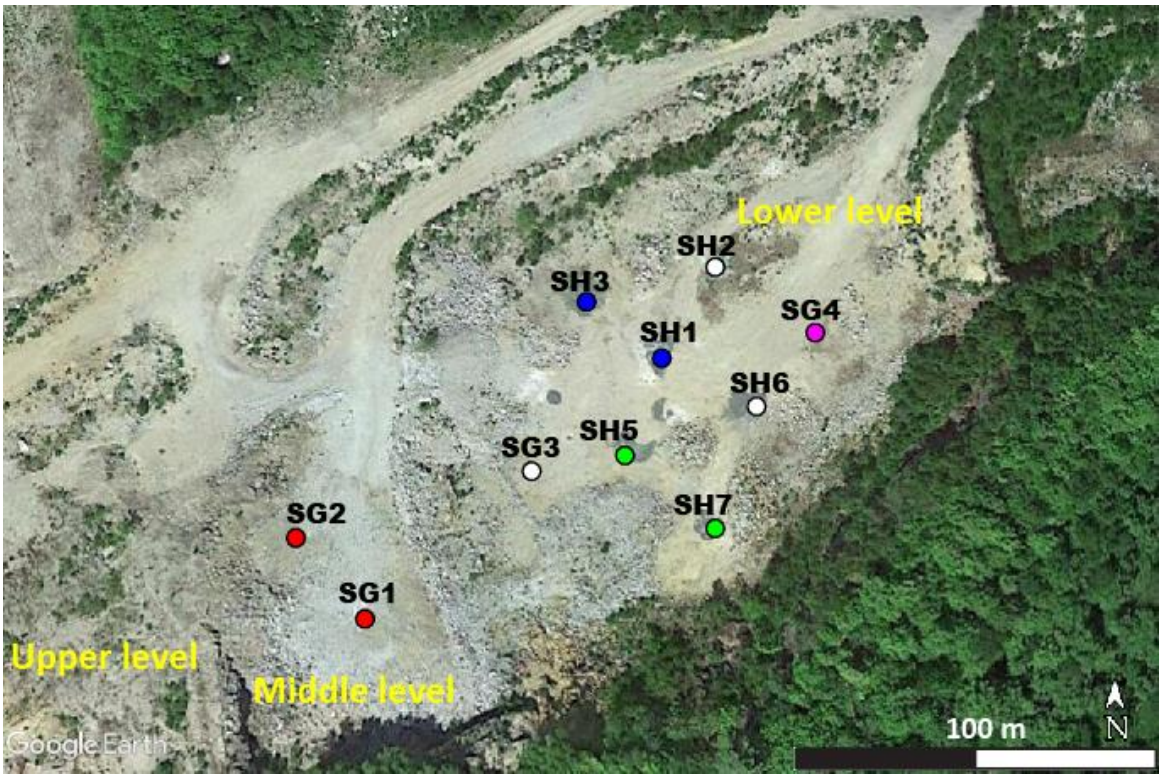

Figure 2. A Google Earth view of the test bed with circles showing the shot locations. ***The circle colors represent different explosive types: ANFO – green, TNT – blue, COMP B – red, Octol – magenta, and aluminized explosives – white.***

Table 1. Explosion characteristics.

Shot	BH depth, m	Depth after loading, m	Centroid depth, m	COMP B, kg	HBX-1, kg	Octol, kg	TNTe yield, kg*
SG1	12.95	11.67	12.31	57.15	-	-	63.4
SG2	13.00	11.81	12.41	57.15	-	-	63.4
SG3	12.65	11.37	12.01	2.04	54.66	-	82.61
SG4	12.70	10.57	11.64	1.59	-	55.02	62.8

* The total TNT equivalent yield was calculated using the following TNT equivalency values for each explosive type: TNT – 1, COMP B – 1.11, HBX-1 – 1.47, Octol – 1.11.

2.2. Drilling and Site Preparation

The map of the test site showing the locations of the shots and the near-source accelerometers is presented in Figure 2. The new boreholes drilled in 2018 are SG1, SG2, SG3, SG4 and SG5 (not shown). All boreholes are 25 cm in diameter with depths between 12 and 13 m. Below is a brief description of the shot boreholes.

Borehole SG1 was drilled in June, 2018 in the middle level of the quarry (Fig. 2) as a part of a separate research project (Designated the Diffusion Experiment) funded by the Defense Threat Reduction Agency under Grant No. HDTRA1-17-1-0040. Because there was approximately 0.75 m of loose debris on top of the bedrock, a PVC casing was installed to prevent the debris from falling into the borehole. This borehole was logged before and after the explosion. After the shot, this borehole was cemented above 2.2 m and tracer gases were injected into the cavity in order to study their migration to the surface through the explosion-generated fracture network (as part of the Diffusion Experiment).

Borehole SG2 is located ~21 m from SG1 on the middle level of the quarry (Fig. 2). The borehole initiates in the bedrock (no overburden). No water was flowing into the borehole through the fractures (tight borehole).

Borehole SG3 is located on the main level of the quarry, where the explosions of GAS2016 experiment were conducted. The borehole depth is ~12 m. There is ~1 m of overburden followed by fractured rock, the competent rock starts below 2 m. The BH produces ~2 gal of water per minute (based on communication with the driller).

Borehole SG4 is also located on the main level of the quarry. The borehole was drilled to a depth of 12 m with approximately 0.75 m of overburden above the bedrock. The casing was set at 2.9 m, the BH is tight below the casing (no water was produced on the day of the drilling).

Borehole SG5 is also on the main level of the quarry. The depth is ~24.3 m (twice the depth for the other shots). On the day of the blasting, the flow rate in the borehole increased. In addition, a step or shift was observed at the bottom of the casing that prevented the charge from being loaded. As a result, no explosion was detonated in SG5 and it was abandoned.

2.3. Blasting

Four explosions were conducted as a part of the experiment (Table 1, Fig. 2). The following explosives were used to conduct the shots: COMP B, HBX-1 and Octol. Pentolite boosters were used to initiate the charges. Four explosive charges were manufactured by Accurate Energetics for this series of experiments. They included two charges of COMP B, one charge of HBX-1 and an Octol charge. Each complete charge was cast in increments or segments. All explosions were recorded using a video camera.

Shot SG1, conducted as a part of the Diffusion Experiment in June 2018, was detonated at the bottom of a 12.95 m borehole (25.08 cm in diameter). The cylindrical charge (125 lbs of COMP

B, 97 cm in length and between 22 – 25 cm in diameter) with two Pentolite boosters placed in a cardboard tube. The total length of the charge, including the base containing the boosters, was approximately 1 m. The borehole was dewatered prior to the charge loading; however, water was flowing back into the hole through the pre-existing fractures upon loading. After the explosive was loaded, the borehole was stemmed with ¾" crushed stone. During the explosion, the casing and a small part of the stemming was ejected (Fig. 4a).

Table 2. Shot locations and origin times.

Shot	Date	Origin time (GMT)	Latitude, °N	Longitude, °W	Depth, m
SG1	06.26.2018	17:36:12.004	44.29371	-71.55516	12.95
SG2	10.24.2018	16:48:19.095	44.29387	-71.55529	13.00
SG3	10.24.2018	16:15:07.038	44.29395	-71.55470	12.65
SG4	10.24.2018	15:47:20.135	44.29426	-71.55395	12.70

Shot SG2 was conducted using a charge identical to SG1 (125 lbs of COMP B, 96 cm in length and 22 – 25 cm in diameter). However, unlike SG1 and other charges of the series, the shot borehole was grouted after the charge was loaded (Fig. 3). The borehole was dewatered prior to loading the charge. Grouting the shot borehole posed considerable difficulties, because the heat from setting concrete could potentially damage the detonator wires. To prevent this from happening, the wires leading from the charge to the surface were protected with insulation foam (Fig. 3a). The grouting process was performed by the drilling crew 1 day before the blasting. The explosion produced a crater (3.5 – 3.7 m in diameter) surrounded by a mound of debris (6 – 8 m in diameter), which was likely formed as a result of the detachment of the upper layers due to spall (Fig. 4b). There was some gas venting producing a fireball. However, the rock underneath the crater appeared to be solid and no large pieces of concrete or the insulated detonator wires were found, suggesting that the integrity of the grout was not significantly affected by the blast.

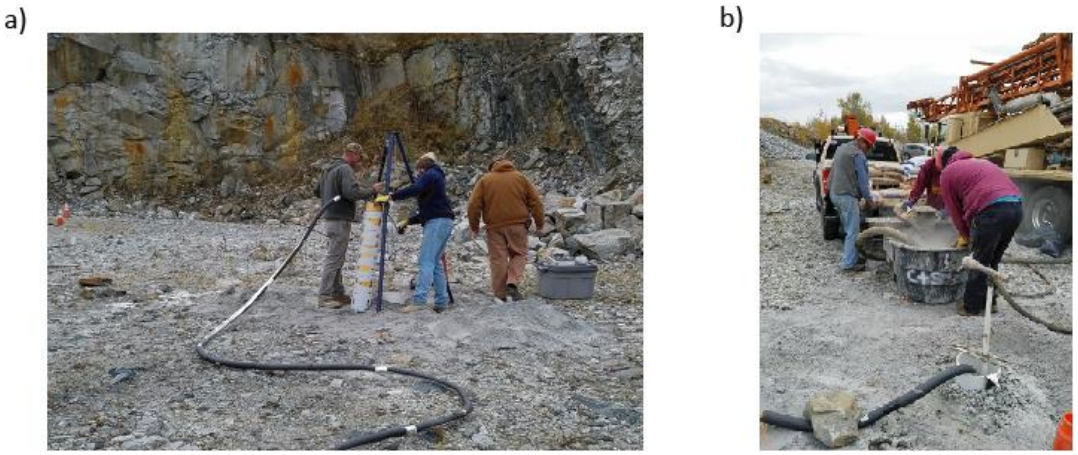

Figure 3. (a) A COMP B charge for Shot SG2 before loading; (b) grouting SG2 charge after loading.

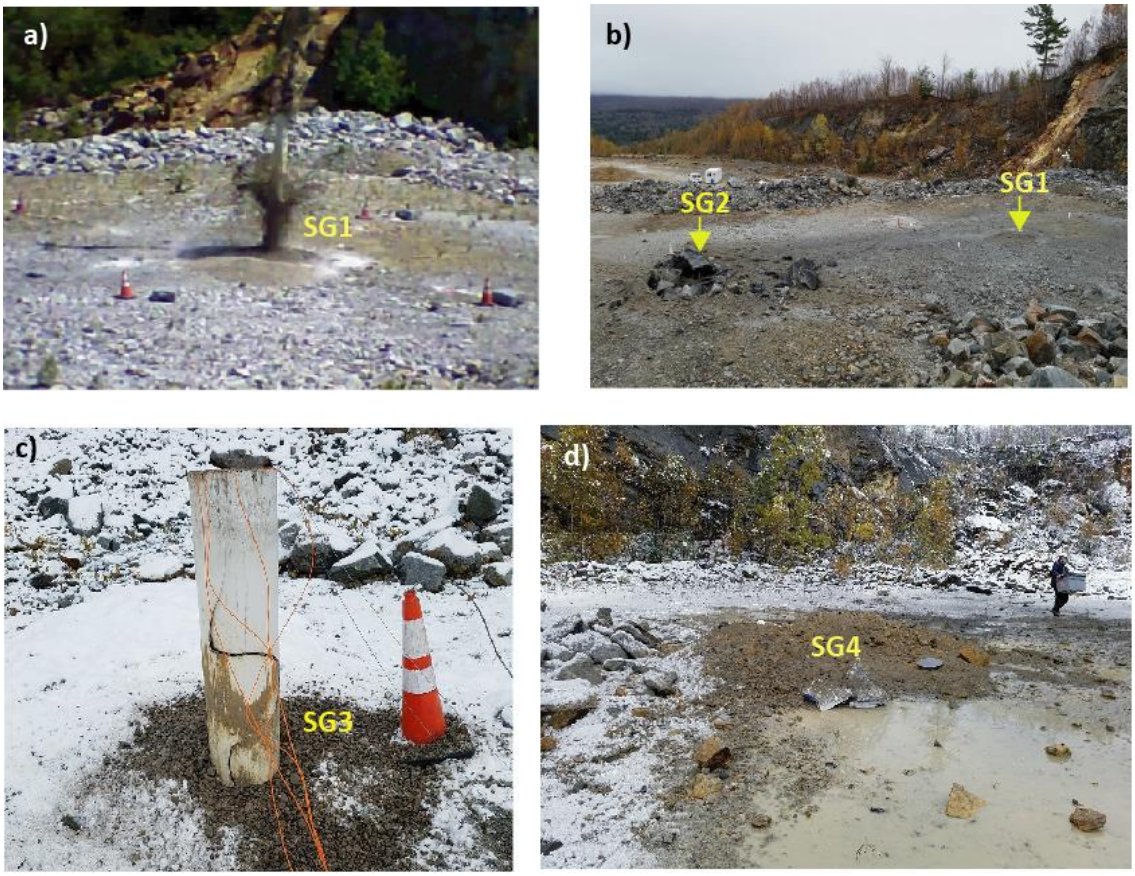

Figure 4. Post-detonation surface effects for: (a) SG1 (ejection of the PVC casing); b) SG2 (cratering) compared to SG1 after clean-up; (c) SG3 (casing ejection); and (d) SG4 (cratering). ***The white substance on the ground is snow.***

Shot SG3 was conducted using HBX-1. Instead of the ordered 125 lbs charge, we received a 120.5 lbs charge split into 9 segments of various weights (with combined length of 98 cm and 20 cm in diameter). Therefore, 4.5 lbs of Pentolite boosters were attached to the bottom of the charge for the total weight of 125 lbs. The blaster was unable to completely dewater the borehole and the charge was loaded with approximately 0.5 – 1 m of water present. After loading the charge, the blasthole was stemmed with ¾ inch stemming (crushed rock pieces used to fill up the loaded borehole). The explosion resulted in ejection of the casing and a small part of the stemming (Fig. 3c).

Shot SG4 was conducted using Octol. The charge received from AES weighed 132.6 lbs (instead of 125 lbs) split into 8 segments of various weights. We removed the 11.3 lbs segment and used the remaining 121.3 lbs of Octol supplemented with 3.5 lbs of Pentolite boosters for the total weight of 124.8 lbs. The combined length of the Octol cylinder was 98 cm (20 cm in diameter). Prior to the shot the borehole was drained and stayed dry as the charge was loaded. After loading the charge, the blasthole was stemmed with ¾" stemming (crushed rock pieces used to fill up the loaded borehole). The shot produced a mound (5 – 5.2 m in diameter, Fig. 4d).

The explosion detonation time was determined using the Weston Inexpensive Timing System (WITS) designed as a loop wire forming a closed circuit with a low voltage recorded with a high sample rate digitizer (RT130). Timing accuracy for the WITS system is 2 ms.

2.4. Velocity of Detonation (VOD) Measurements

The velocity of detonation (VOD) was recorded using a MREL HandiTrap II VODR. A resistance wire is taped to the booster and lowered down the hole. As the detonation wave propagates up the borehole, the resistance wire is melted and the recorder measures the decreasing resistance at 1 million samples per second. The resistance was then converted to distance and a velocity calculated.

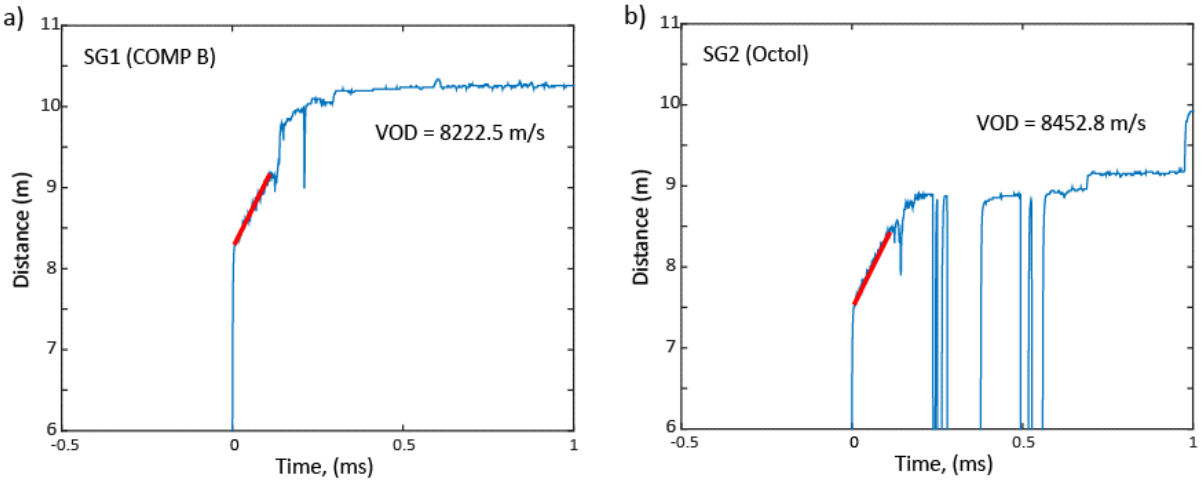

Figure 5. VOD measurements for (a) SG1 (COMP B) and (b) SG4 (Octol). ***The slope of the red line segment indicates the velocity.***

Table 3. Detonation parameters of the explosives used in the experiment.

Explosive type	ρ (kg/m^3)	Q^* (MJ/kg)	$n^\dagger$ (mol/kg)	T_{CJ} * (°K)	VOD (m/s) *		Estimated p_{CJ} (GPa)
					Estimated	Measured	
TNT	1597	5.588	25.8	2935	6950	7025	19.8
Tritonal (TNT/Al 80/20)	1740	8.564	19.1	5196	6700	6673	19.5
ANFO	880	4.183	43.8	2303	5410	4958	7.5
ANFO/Al 80/20	-	6.713	34.2	4067	-	4202	-
COMP B (RDX/TNT 60/40)	1681	6202	30.9	2780	8080	8222	28.4
HBX-1 (RDX/TNT/Al/wax 40/38/17/5)	1810	8421	21.4	5218	7600	-	26.8
Octol (HMX/TNT 75/25)	1702	6209	31.8	2589	8570	8453	33.4

* Parameters Q, VOD and p_{CJ} were calculated using BKW code (Mader, 1967)
† Calculated using Akhavan, 2004.

We recorded the VODR measurements for all four shots; however two of the shots produced very noisy results and are not presented here. Figure 5 shows the plots of the wire length as a function of time for Shots SG1 and SG4. The VOD is calculated as a slope of the line during the stationary detonation. Shot SG1 (COMP B in stemmed borehole) detonated with a VOD of ~8.22 km/s, whereas the VOD for the Octol charge was 8.45 km/s. These values are within the range for the corresponding explosive types. Table 4 summarizes the measured and calculated VOD as well as other characteristics of the explosives used in the experiment.

2.5. Seismic and Acoustic Data Acquisition

A network of 3-component seismic instruments was deployed to monitor the explosions (Fig. 6). The network included 25 short-period seismometers and 10 accelerometers. The waveforms were recorded using Reftek 130 (RT130) data loggers.

In addition to accelerometers and short-period seismometers, 10 sites were equipped with acoustic sensors. The acoustic measurements were made using Hyperion IFS-5311 seismically-decoupled infrasound sensors with 100 Pa maximum pressure range. The sensors were recorded on RefTek 130S digitizers at 500 or 1000 samples per second (sps). The acoustic sensors were covered with foldable mesh domes to reduce wind noise (Fig. 7). The objective of their deployment was to measure the acoustic component of underground explosions in hard rock. A fully contained and confined explosion will not generate an acoustic signal from the blast itself, although there may be a high-frequency signal generated by the initiation system and/or a lower frequency signal resulting from the spall.

In the near-field, five Endevco 25g accelerometers and five TerraTech 5g accelerometers were installed in close proximity to the explosions to record the near source ground motions (Fig. 6a). Notice that the locations of the accelerometer network for the June and October deployments are different to accommodate different shot locations. The instruments located at the test bed were grouted. Near-field sites NS08 (June deployment) and NG06 and NG10 (October deployment) had co-located acoustic sensors. The near-source accelerometers recorded at a sampling rate of 1000 samples per second.

Thirteen near-source short-period stations were installed on the property belonging to Pike Industries at distances between 0.3–1.2 km with approximately 200 m intervals at various azimuths (Fig. 6b). Stations NE01, NE02, NE03, NE04, and SE02 have additional acoustic sensors. All short period stations located in the quarry were recording continuously with a sampling rate of 500 samples per second. Twelve short-period stations were installed off the quarry property at local distances between 1.2 km and 8 km (Fig. 6a). All of these stations except Station GOUL were equipped with PASSCAL BIHO boxes with 2 Hz Sercel L22 2Hz 3C sensors. Stations GOUL, ARR2 and WARR were also equipped with acoustic sensors. All these stations were recording continuously with a sampling rate of 500 samples per second.

The acoustic measurements were made using Hyperion IFS-5311 seismically-decoupled infrasound sensors with 100 Pa maximum pressure range (Fig. 7). The sensors were recorded on

RefTek 130S digitizers at 500 or 1000 samples per second (sps). The objective of their deployment was to measure the acoustic component of underground explosions in hard rock.

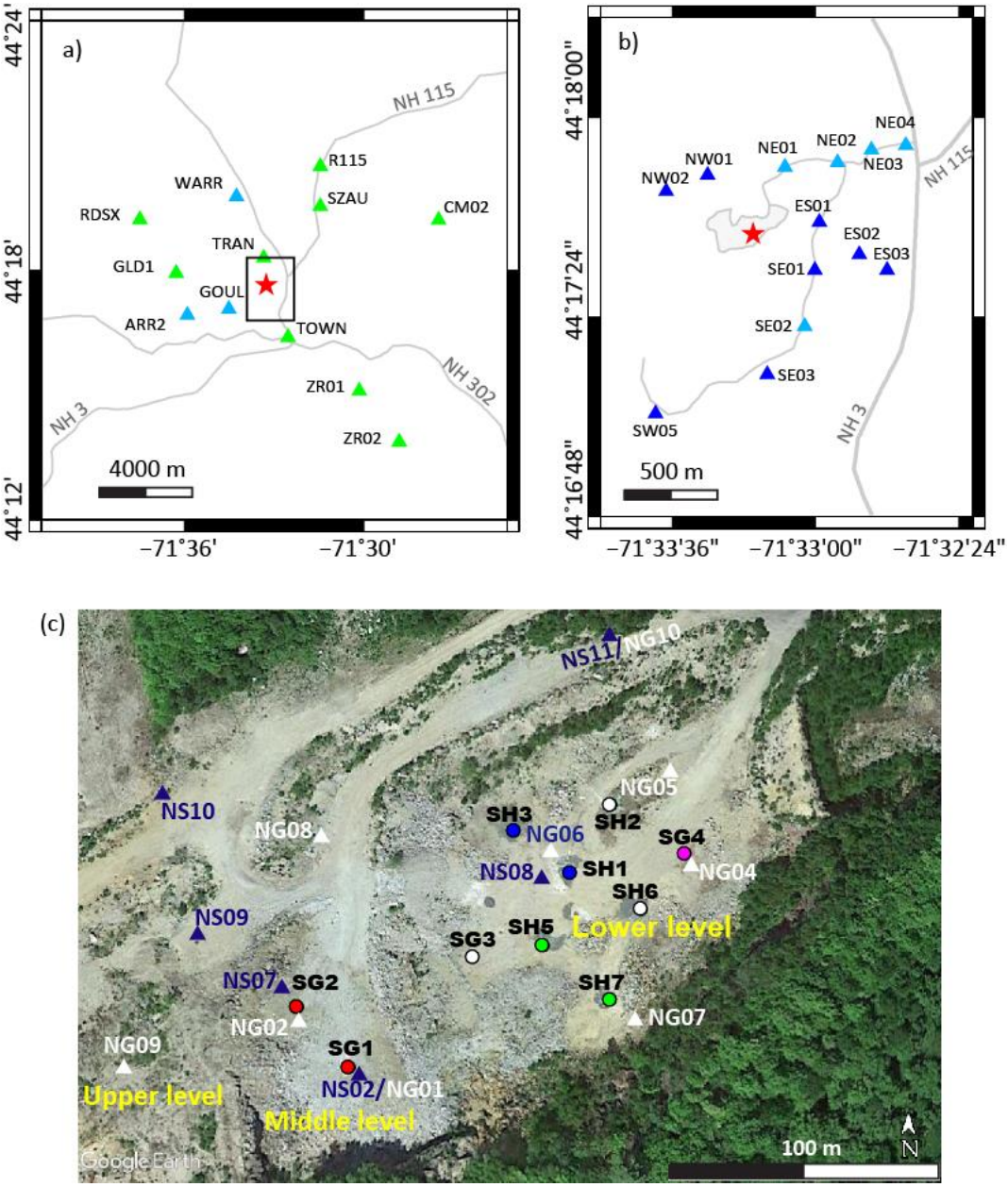

Figure 6. (a) Seismic stations deployed at local distances from the explosions near Twin Mountain, New Hampshire (USA). *The green triangles show the seismic stations, the light blue triangles show the seismic and acoustic sites. The stars show the test site location. The rectangle is enlarged in (b).* (b) The near-source network of the short-period seismometers. *The blue triangles show the stations with short-period seismic sensors (L22) only, whereas the light blue triangles show the stations equipped with both seismic (L4) and acoustic (Hyperion IFS-5311) sensors.* (c) Test bed showing the shot locations and the near-source accelerometers (blue triangles – accelerometers deployed in June 2018, white triangles – deployed in October 2018).

Figure 7. Station WARR equipped with L-4 seismometer and an acoustic sensor (Hyperion IFS-5311). ***The acoustic sensor is covered with a wind noise-reducing dome.***

2.6. Seismic and Acoustic Data

2.6.1. Accelerometer Data. The near-source accelerometers were placed at distances between 0.5 and 200 m from the sources. Figure 8 shows the spall records from 4 explosions conducted in 2016 (left column, Fig. 8a-d) and 4 explosions conducted in 2018 (right column, Fig. 8e-h).

The near-source records show the impulsive shock wave arrivals, followed by a period of downward acceleration (dwell), and then a series of spikes resulting from slapdown(s). SG1 (COMP B in a borehole containing water) produced the highest amplitudes for the first impulses. Shots SG1 and SG2 were conducted using identical charges, however the amplitude of the first peak for SG1 is more than twice the amplitude for SG2.

Shot SG2 resulted in the ground failure and produced a crater/retarc. The accelerogram shows a complex signal starting about 0.04 s after the first peak, apparently due to the venting and the ground failure. In the end of the motion the accelerometer became airborne, which can be observed from very long period intervals of upward and downward acceleration.

Shot SG4 also resulted in the ground failure and ejection of the accelerometer. In this case the high-amplitude signal, apparently related to the venting and ground failure starts close to 0.1 s. Notice that in both cases the ground failure starts long after the passage of the shock wave and after the dwell phase (in the case of SG4), which indicates that the cratering was produced as a result of the late time damage rather than caused by the shock wave.

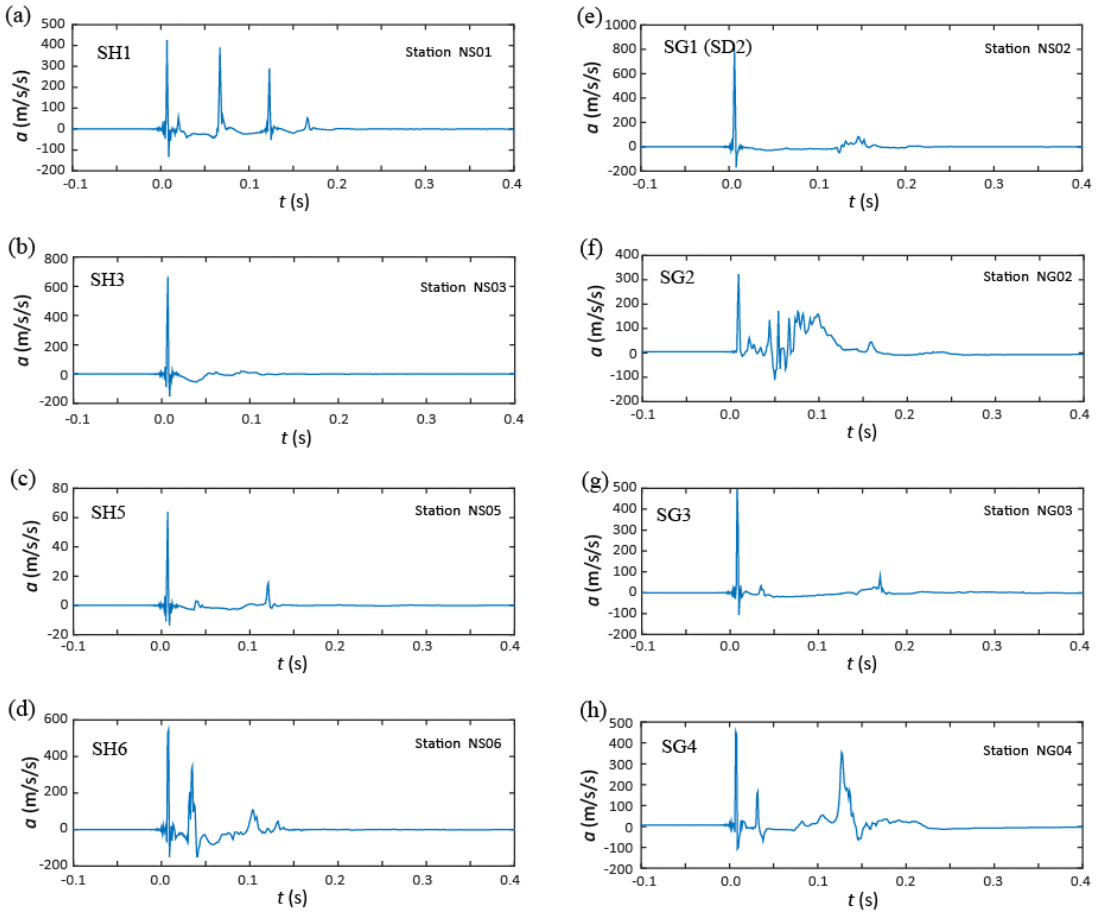

Figure 8. Near-source accelerometer records for: (a) SH1, (b) SH3, (c) SH5, (d) SH6, (e) SH1, (f) SH3, (g) SH5, (h) SH6. ***The accelerometers were located between 1 – 1.5 m from their respective shot boreholes.***

2.6.2. Seismic Data. A dense geophone network was installed around the quarry. The near-source network consisted of 13 short-period 3C stations. All these stations were equipped with L-22 geophones at a sampling rate of 500 samples per second. Stations ZR01, ZR02, and CM02 (Fig. 6a) are located in the rugged area of National Forest separated from the test site by a river valley. The area to the west and north of the test site is somewhat less rugged. The stations in that area were located in the residential properties, while two of the sites, TOWN and TRAN, were located on the municipal property belonging to the Town of Twin Mountain near the town hall and the transfer station, respectively.

Figure 9 shows the waveform comparison between shots SG1 and SG2 (two COMP B shots, left column) and SH1 (TNT, 2016) and SG4 (Octol, 2018, right column) for stations GOUL, ARR2, SZAU, R115, and RDSX) located between 2 and 6.3 km from the sources. As expected, the SNR degrades with the increase in range.

Figure 10 shows the waveforms from the four explosions recorded by station GOUL located approximately 2 km from the sources. Notice the *Rg* amplitude reduction for the Octol shot (SG4) compared to other events.

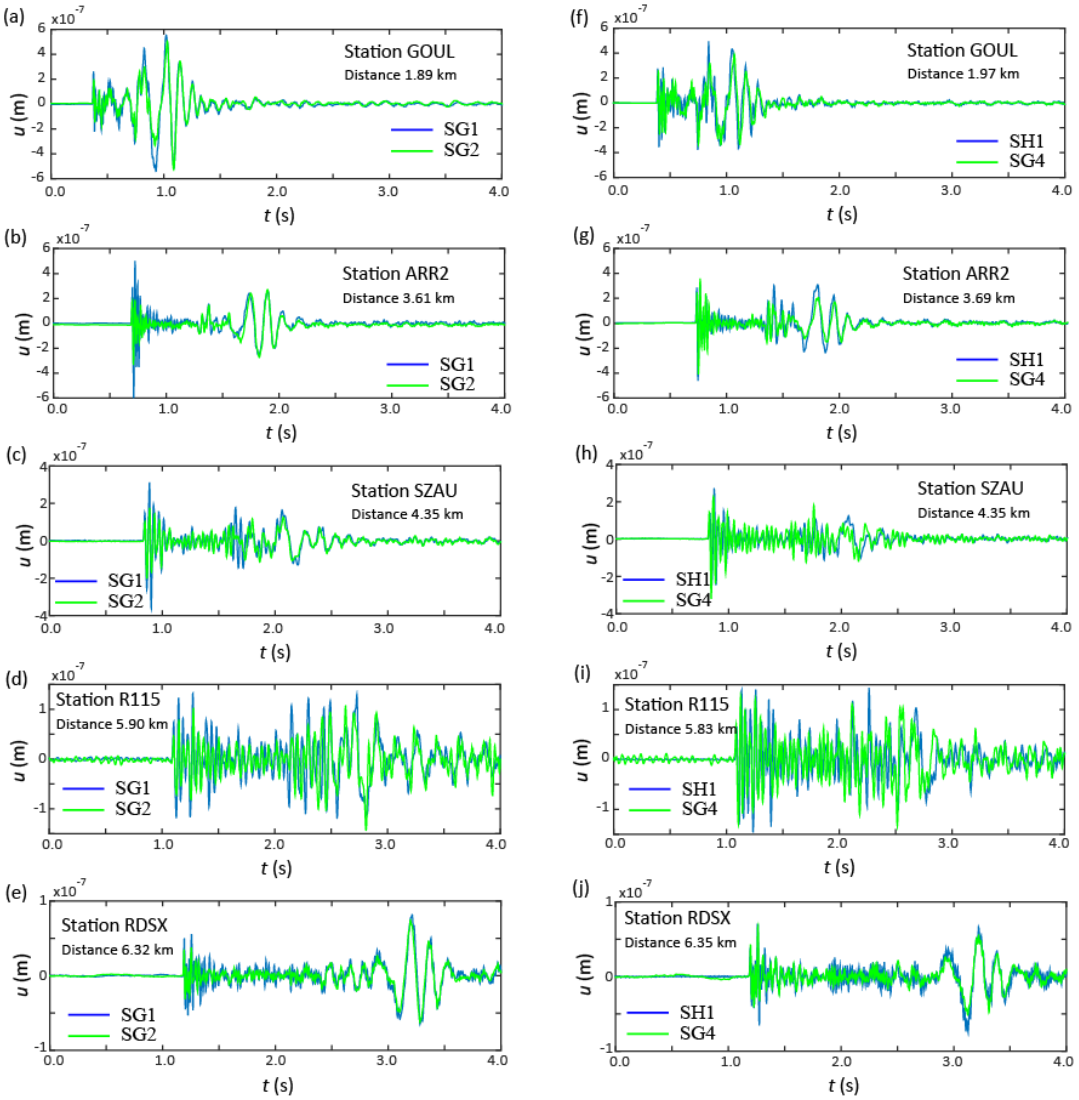

Figure 9. Left column: comparison between two COMP B shots – SG1 (grouted borehole) and SG2 (stemmed borehole containing water) for the following stations: (a) GOUL, (b) ARR2, (c) SZAU, (d) R115, and (e) RDSX. Right column: comparison between the TNT shot (SH1) and the Octol shot (SG4), both in dry stemmed boreholes for the following stations: (f) GOUL, (g) ARR2, (h) SZAU, (i) R115, and (j) RDSX.

Figure 11 shows the vertical components of the seismic traces from station ARR2 for all shots performed in 2016 and 2018. The amplitudes of *Rg* phases decrease as the VOD increases. This effect is less pronounced for the shots in boreholes containing water (e.g. SH7 vs SH3). The amplitude increase due to water presence in the shot borehole is more pronounced for higher VOD explosives (TNT) compared to low-VOD ANFO. *P* wave amplitudes for the grouted shot in a dry borehole (SG1) are significantly lower than for the shot in water-containing stemmed borehole

(SG2). *P* amplitudes from the Octol shot (SG4) are higher than for the TNT shot (SH1), whereas the *Rg* amplitudes are consistently lower (for all stations with discernible *Rg*) for SG4. It is interesting that there is no amplitude increase observed for the shots with considerable surface damage (cratered shots) compared to fully contained shots with little or no surface damage.

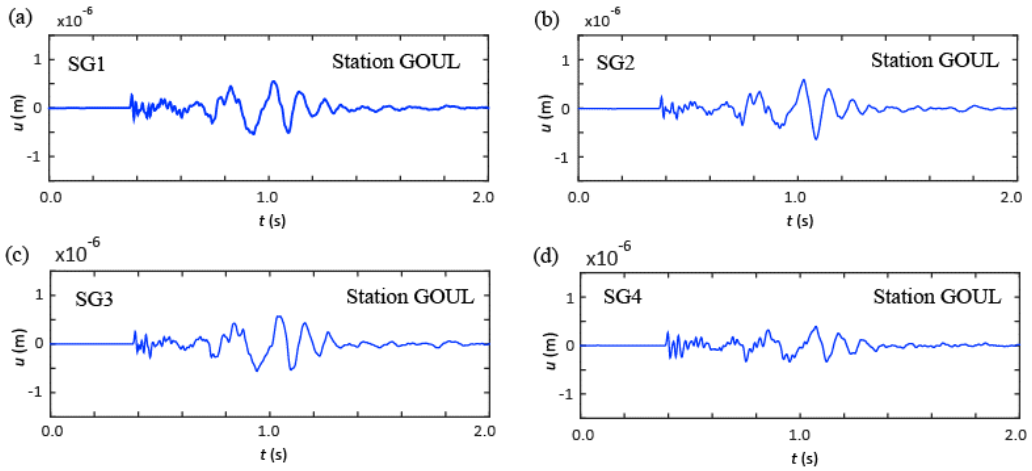

Figure 10. Vertical components of the velocity seismograms recorded by short-period station GOUL located approximately 2 km from the sources for: (a) SG1, (b) SG2, (c) SG3, and (d) SG4.

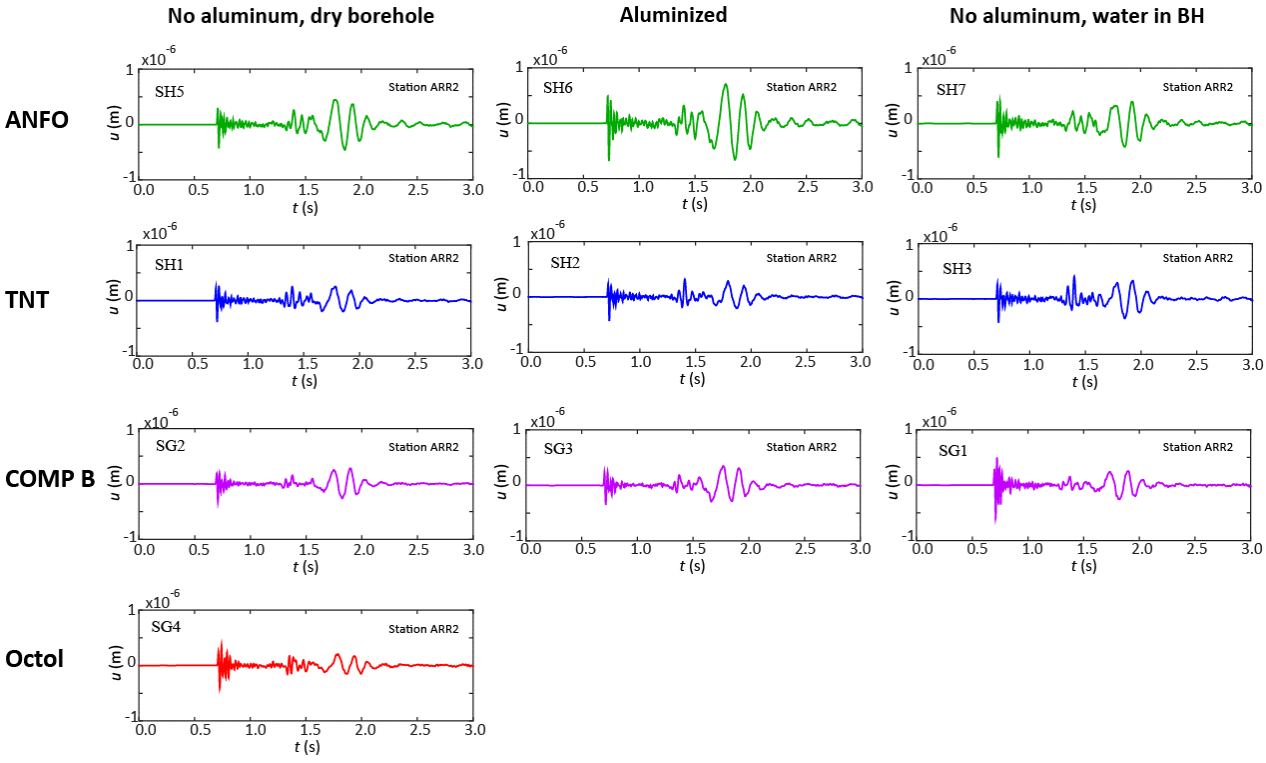

Figure 11. Vertical components of the displacement seismograms from short-period station ARR2 located 3.7 km from the source array.

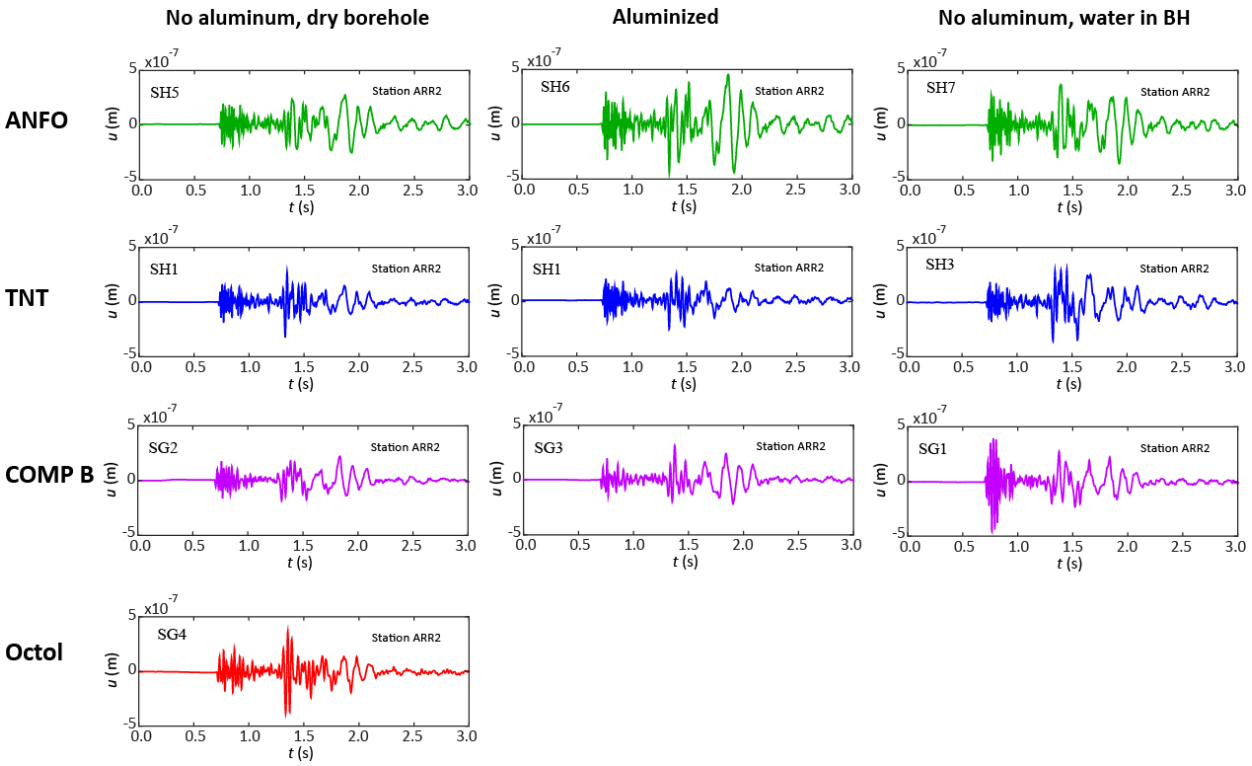

Figure 12. Transverse components of the displacement seismograms from short-period station ARR2 located 3.7 km from the source array.

The transverse components for station ARR2 are plotted in Figure 12. Notice the complexity of the signal in the *S*-wave window. For instance, the low-frequency high-amplitude arrival in the *S*-wave window, which is more pronounced for the ANFO-based shots, could be related to the *Rg* scattering. Interestingly, the Octol shot (SG4) has the highest amplitude in the *S*-wave window for this station.

Amplitude increase for aluminized explosives of the same weight and higher yield (ANFO – ANFO/Al, TNT – Tritonal, and COMP B – HBX-1 pairs) is observed only for the ANFO – ANFO/Al pair. No significant amplitude increase for Tritonal vs TNT and for HBX-1 vs COMP B was observed.

Figure 13 shows the displacement spectra for all shots of the series. The spectra for each event are averaged over three stations located at similar distances from the sources (R115, ZR01, and RDSX). Shots conducted using ANFO (SH5 and SH7) as well as the TNT shot detonated in water-filled borehole (SH3) have higher amplitudes, particularly in the low-frequency part of the spectra. The explosives with faster VOD (Octol and COMP B) as well as TNT in dry borehole resulted in reduced amplitudes in the low-frequency part of the spectrum. With the exception of the COMP B shot in the grouted borehole (SG2), no amplitude reduction in the high-frequency part of the spectrum is observed.

Thus, we observe an amplitude increase at low frequencies for explosions with slower VOD and higher gas volume. Similar amplitude increase is observed for the explosions conducted in the

water-filled boreholes. These observations support the previous findings from New England Damage Experiment (e.g. Stroujkova, 2012, 2015b) suggesting an increase in the low frequency amplitudes for the explosions with higher amount of the gaseous products.

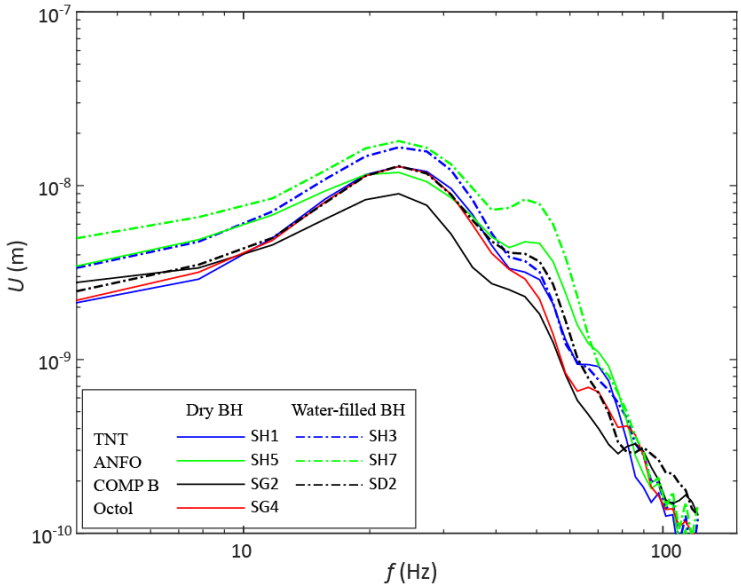

Figure 13. *P*-wave spectra averaged over several local stations located at similar distances from the sources: R115 – distance 5.8 km, ZR01 – distance 6.3 km, and RDSX – distance 6.4 km.

2.6.3. Acoustic Data. A fully contained and confined explosion will not generate an acoustic signal from the blast itself, although there may be a high-frequency signal generated by the initiation system and/or a lower frequency signal resulting from the spall. A non-electric shock tube initiation was utilized in this experiment, which creates a short-duration peak a few milliseconds before the explosive detonates. High sample rate recordings are needed to differentiate this initiation signal from an explosion generation signal caused by incomplete containment or confinement. The signal of interest for this research is the spall-generated pressure pulse. This is a lower frequency pulse created by the ground heaving vertically, from the shock wave passage and interaction with the free surface, and the subsequent relaxation back in a downward direction. The amplitude and duration of this signal provide information on a combination of the charge yield, charge depth, and material properties. This information can be utilized in yield estimation and event forensics analysis.

Figure 14 and Figure 15 show examples of the overpressures recorded using the infrasound sensors. Figure 14 shows the records of the fully confined explosion (SG1) recorded with 4 stations located in the quarry at distances between 494 m and 1067 m from the source. Figure 15 shows the recordings of 4 shots conducted in 2018 at Station NE03, located approximately 800 m from the sources. Notice that the vertical scale for shots SG2 and SG4 is 10 times the scale for SG1 and SG3. SG2 and SG4 have significantly higher amplitudes because these shots vented.

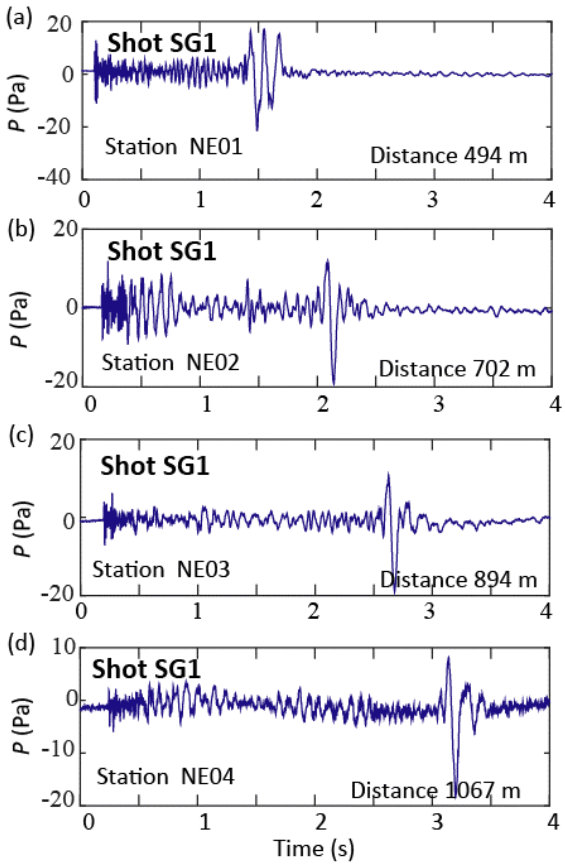

Figure 14. Overpressures for shot SG1 recorded by stations NE01 – NE04.

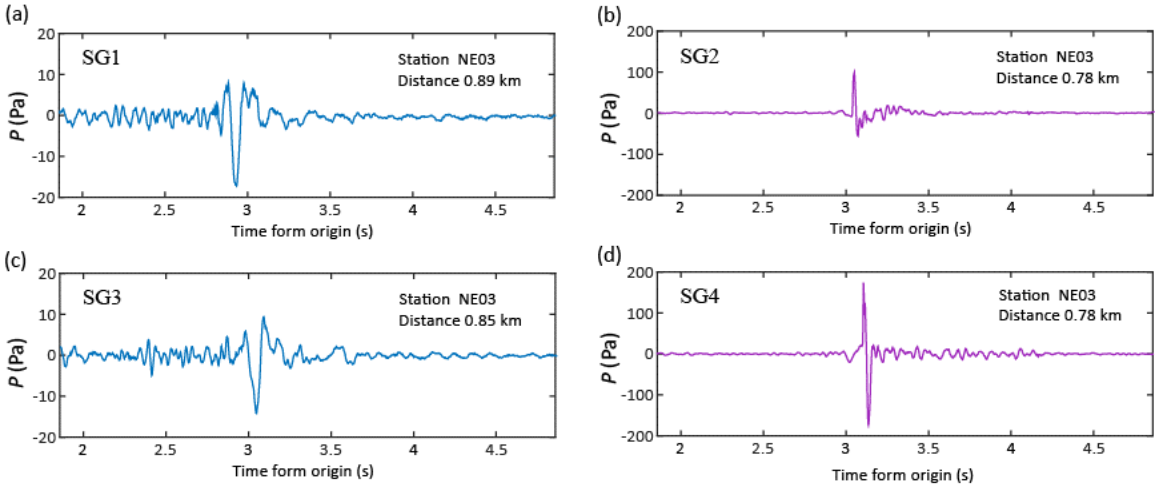

Figure 15. Overpressures recorded by station NE03 for shots: (a) SG1, (b) SG2, (c) SG3, and (d) SG4.

2.7. Conclusions

A series of explosion experiments was conducted in New Hampshire in 2018. The purpose of the experiment was to study the seismic signatures of the explosion sources using different explosive types. The experiment confirmed reduced *P* and *Rg* amplitudes for low-gas, high-VOD explosives (TNT, COMP B, and Octol) in comparison with high-gas, low-VOD explosives (ANFO). The amplitude reduction is more pronounced in the low-frequency band (1 – 10 Hz).

Detonating charges in boreholes containing water results in seismic amplitude increase by a factor of up to 1.5. The amplitude increase is more pronounced at high frequencies (10 – 100 Hz). The presence of water also results in more extensive fracturing and higher non-isotropic source component. Detonation of a COMP B charge in a grouted borehole produced a crater and lower seismic amplitudes than the detonation of an identical charge in a stemmed borehole containing water. Detonation of the Octol charge also resulted in a crater formation.

Comparison between COMP B and HBX-1 shows that the aluminized HBX-1 charge of higher design yield produced similar amplitude as the lower-yield COMP B charge.

3. POST-EXPLOSION SITE CHARACTERIZATION

3.1. Introduction

This chapter discusses the results of the post-explosion geophysical site characterization conducted as a part of GAS2018 experiment. This effort is a continuation of the post-shock rock characterization conducted as a part of GAS2016 experiment. In 2018 the well logging survey was conducted in two blast holes. The purpose of the well logging was to characterize the damage created by the underground explosions and to relate it to the radiated seismic waves.

3.2. Well Logging

Well logging was performed as a part of the 2018 experiment by Hager Geoscience. After completion of the explosive experiment two of the four shot boreholes (SG1 and SG3) were evacuated in order to study the damage in the explosive cavities and along the boreholes. Shots SG2 and SG4 cratered resulting in a significant surface damage; therefore, it was impossible to drill back into these shot holes. Figure 16 summarizes the availability of the well logs for both the 2016 and 2018 experiment series.

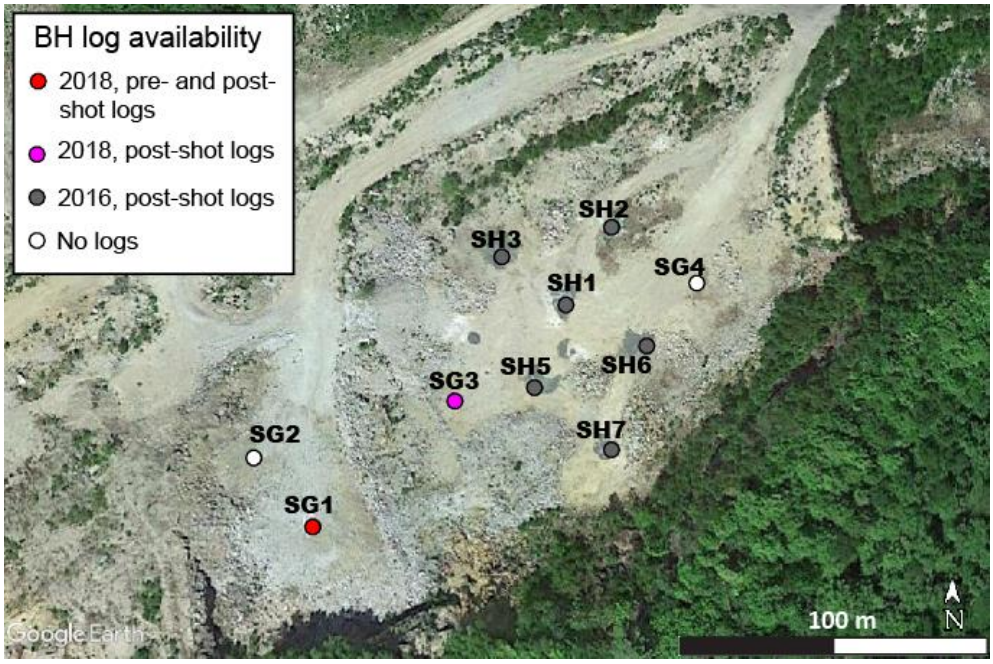

Figure 16. Map of the experiment site in Carroll, NH, showing the locations of the de-stemmed shot boreholes (red, magenta, and grey circles), where geophysical logging (ATV, OTV, caliper and video logs) was conducted. *White circles show the locations of the shots resulting in significant surface damage, which could not be re-drilled.*

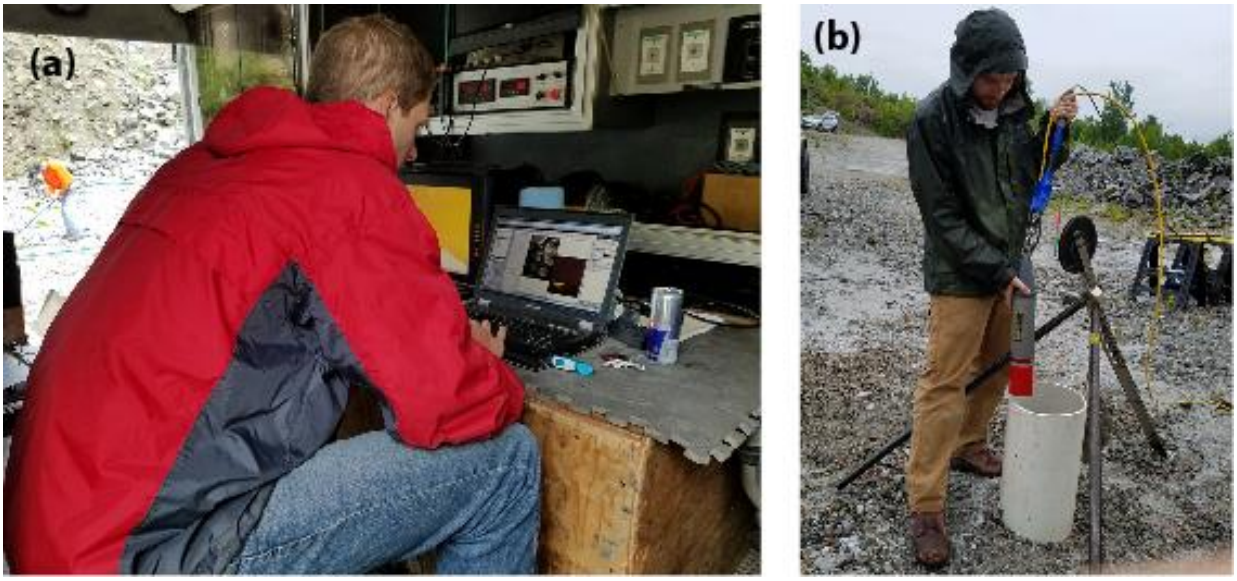

Figure 17. (a) Well logging of SG1 borehole. (b) Sonar tool.

The well logging included down-hole camera, acoustic televiewer (ATV), optical televiewer (OTV) and caliper logs. The caliper probe produces a continuous record of the borehole diameter using three mechanically coupled arms in contact with the borehole wall. Changes in borehole diameter are related to fracturing or breakout along the borehole wall. Because borehole diameter commonly affects log response, the caliper log is useful in the analysis of other geophysical logs. The sampling interval for the logging was 1.2 cm, at a logging rate of approximately 4.5 meters per minute. The OTV and ATV logs were used to visualize the surface of the boreholes and the damage caused by the explosions. The OTV produces a continuous oriented 360° image of the borehole wall using an optical imaging system. Imaging the cavities produced by the explosions was performed by using the ATV and caliper. Below we summarize the logging results for each borehole.

SG1: 57.2 kg of COMP B in a water-filled stemmed borehole (63.4 kg TNTe). OTV (pre- and post-shot) and caliper logs for SG1 are shown in Figure 18 and Figure 19, respectively. The rock in the borehole is fine-grained granite/gneiss. The predominant orientation of rock discontinuities has a NE-SW strike and moderate to high-angle dip to the NW. A small set of fractures strikes NNE and dips at high angles to the SE. Pre-existing fractures are noted around 3m, 6m, and below 10m. Vertical fractures extending from the surface to the cavity are clearly seen in the post-shot OTV log. The step-like characteristic of the vertical fractures is due to the diversion of the vertical fractures by foliation planes. The strike azimuths of the vertical fractures range from approximately 39° to 47°. The cavity is observed below 10.1 m and widens below 11 m. The cavity volume (0.349 m^3) is similar to the one produced by the TNT shot (SH1 – 0.373 m^3). Both cavities (SG1 and SH1) may not have been completely evacuated because the charge bottom appears to be below the evacuated cavity. This cavity was later sealed with concrete and used for tracer gas studies.

SG3: 57.2 kg of HBX-1 in a water-filled stemmed borehole (82.6 kg TNTe). OTV and caliper logs for SH2 are shown in Figure 18 and Figure 19 respectively. The rock is similar in composition and texture to that in SG1. Foliation and banding are the predominant rock fabric. Step-like vertical blast-induced fractures are visible up to the bottom of the casing. Vertical fractures extending from the surface to the cavity are likely blast related. The cavity is observed below 10.1 m. The cavity volume (0.342 m^3) is comparable to the other cavities produced by other high explosive shots (TNT – 0.373 m^3, Tritonal – 0.363 m^3, COMP B – 0.349 m^3). Notice that the HBX-1 charge has higher yield (Table 1, Table 2) than non-aluminized charges (TNT, COMP B). Both cavities shown here (SG1 and SG3) may not have been completely evacuated because the charge bottom appears to be below the evacuated cavity.

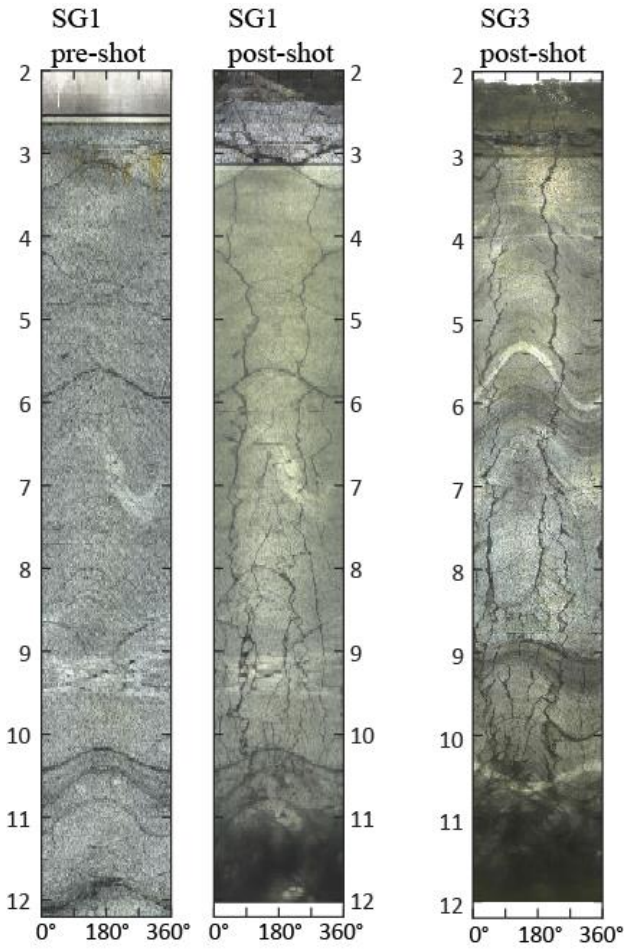

Figure 18. **OTV logs For SG1 (before and after the shot) and SG3 (after the shot).**

Six other boreholes located in the quarry were logged as a part of the previous experiment (GAS2016; Stroujkova, 2018a). Five of these boreholes were used as the blast holes, and one was an analysis borehole. The dominant rock type observed in the boreholes during well logging is fine-grained granite or gneiss with bands of mafic minerals including possible amphibolites at some locations/depths. The fractures identified from the ATV/OTV logs have predominant dip azimuths ranging between 285-315º, and the mean dip of approximately 53º. Full waveform sonic logging of BH1 indicated compressional (*P*) wave velocities of 4300 – 5300 m/s and shear wave velocities of 2500 – 2800 m/s. Normal Formation Resistivity logging of BH1 shows the resistivity

of 1000 – 2000 Ohm-m between the water table and the depth of approximately 10.6 m. Below this depth the resistivity gradually increases to 8000 – 10,000 Ohm-m at a depth of 16.8 m (for the electrode spacing of 0.8 – 1.6 m).

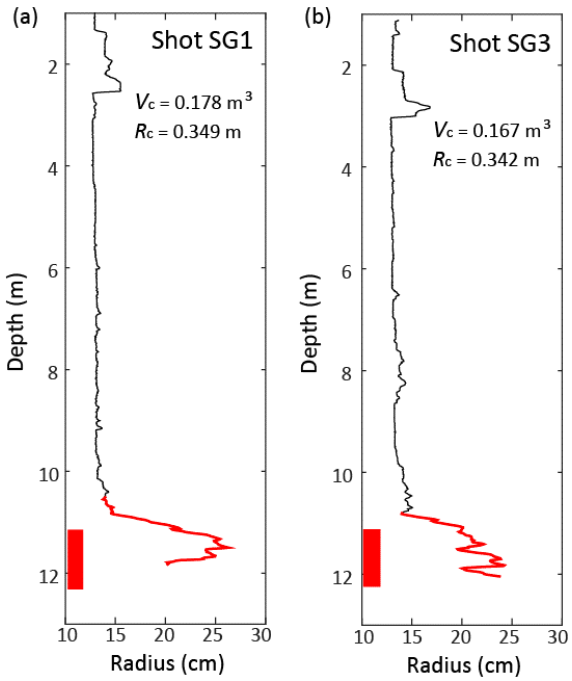

Figure 19. Post-shot caliper logs for (a) SG1 and (b) SG3. Estimated cavity volumes (V_c) and effective cavity radii (R_c) are shown.

3.3. Conclusions

Post-shot well logging was performed in the shot boreholes in order to quantify post-explosion rock damage. The post-explosion changes to the rock include: 1) formation of the cavity and crush zone during the explosive detonation; 2) enhancement of the pre-existing fractures and joints; 3) spall zone damage produced due to the shock wave interaction with the free surface; and 4) vertical or high-angle fractures extending along the boreholes.

All explosions produced cavities (voids) around the charge. The volumes of the cavities produced by the high explosive charges are: 0.349 m^3 for COMP B and 0.342 m^3 for HBX-1 (compare 0.373 m^3 for TNT and 0.363 m^3 for Tritonal). The cavity sizes are consistent with previously reported results for small chemical explosions in granite (e.g. Stroujkova et al, 2016).

In addition to creating cavities around the working point, the explosions created extended macro-fractures. Low-angle shallow fractures, possibly related to spall, are observed in all boreholes. Other fractures related to the pre-existing fractures are also common. In addition to reactivating pre-existing fractures, vertical or near-vertical fractures extend above the blast cavities. Our previous experiments (e.g. NEDE; Martin et al, 2012) show that the fractures along the borehole are ubiquitous for the small chemical explosions. The fractures observed during NEDE, however,

terminate at greater depth due to the presence of large sub-horizontal joints. The site used in GAS2016 experiment did not have the large sub-horizontal joints, therefore the explosion-related fractures in some cases extended to the surface. ANFO–based explosions produced longer fractures with larger apertures. Shot SH3 conducted in a water-filled borehole also resulted in larger fractures than the TNT-based shots in dry boreholes (SH1 and SH2). The increase in the loading rate for the explosives with high velocity of detonation, with subsequent increase in dynamic strength (e.g. Ashby and Sammis, 1990; Sammis, 2011), as well as the increase of the pore pressure due to larger volume of the gaseous products are the main factors responsible for the larger apertures and the extent of the explosion-related fractures for the ANFO-based explosives.

4. RADIATION PATTERN AND FOCAL MECHANISM STUDY

4.1. Introduction

The results of GAS2016 experiments (e.g. Stroujkova, 2018a) have shown that the radiation patterns of the *P*-waves are different for the low-pass (1 – 10 Hz) and high-pass (10 – 100 Hz) filtered waveforms. The asymmetry of the radiation patterns indicates the presence of non-zero off-diagonal terms of the moment tensor (M_{xz} and M_{yz}). The amplitude of the seismic component attributed to the off-diagonal moment tensor (MT) elements was shown to be as large as 15 – 16% of the isotropic moment. These results were based on the analysis of the six events conducted using TNT- and ANFO-based explosives. In this study we combine the data from GAS2016 with the data from new explosions detonated using COMP B and Octol. The addition of these explosives allows us to examine the effect of the VOD on seismic radiation. In this chapter, we examine the azimuthal patterns of *P* and *Rg* phases. Adding *Rg* phases to the moment tensor inversion helps to constrain the strength of the vertical dipole with respect to the horizontal dipole.

4.2. Radiation Patterns

Azimuthal variations of the explosion-generated seismic amplitudes are determined by the event source processes as well as by the propagation effects. To eliminate the propagation effects, we used the amplitude ratios with respect to a reference event instead of the absolute amplitudes. Following Stroujkova (2018a), Shot SH1 was used as a reference. *P*-wave amplitudes were measured from the first positive peaks because this phase is the least affected by the interactions with the medium. *Rg* amplitudes were measured from the peak of the trace envelopes.

P-wave amplitude ratios with respect to SH1 are plotted as a function of azimuth in Figure 20. The amplitudes were extracted from the waveforms filtered in two different frequency bands: a) a low-frequency band (1 – 10 Hz), and b) a high-frequency band (10 – 100 Hz). Frequencies below 10 Hz belong to the flat portion of the spectra, while frequencies above 15 Hz include the corner frequency and the high-frequency roll-off. *P*-wave amplitudes were measured using the first positive peaks because this phase is the least affected by the interactions with the medium. According to Figure 20a, *P*-wave amplitude ratios between SH2 and SH1 are close to 1 for all azimuths, whereas the ratios for the ANFO shot (SH5) and the shots conducted in water-filled boreholes (SH3, SG1) are greater than 1 for most directions and show considerable azimuthal variations with respect to SH1.

The amplitude ratios for shots SH3, SH5, SG1, and SG2 with respect to SH1 are higher in the low-frequency range (1 – 10 Hz) than above 10 Hz. The amplitude ratios between SG4 (Octol) and SH1 show the opposite trend. The radiation patterns appear to be different between the low and high frequency bands for some events suggesting that different source mechanisms could be dominant at different frequencies.

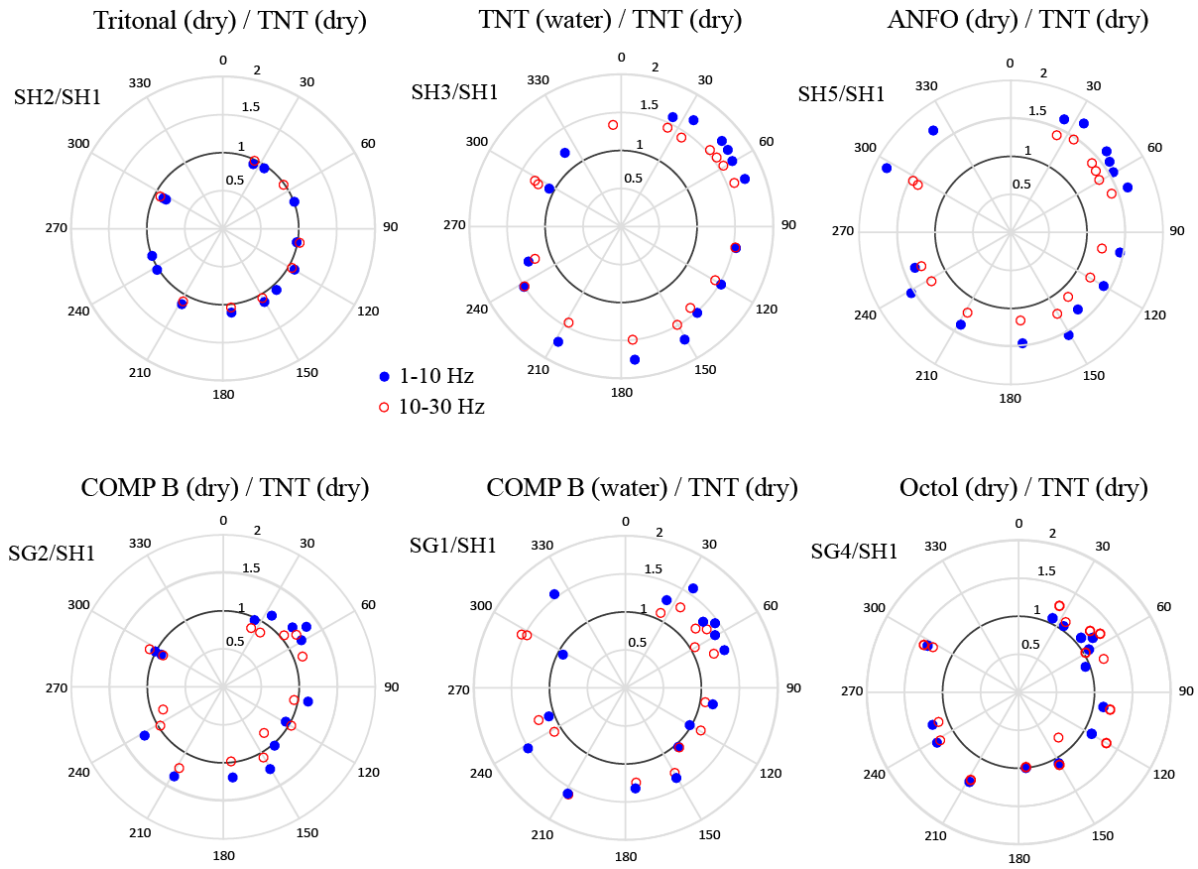

Figure 20. Ratios between the *P*-wave amplitudes of the first positive peak plotted as a function of the station azimuths for the event pairs: (a) SH2/SH1; (b) SH3/SH1, (c) SH5/ SH1, (d) SG2/SH1, (e) SG1/SH1, and (f) SG4/SH1. *The amplitudes were extracted from the waveforms filtered between 1 – 10 Hz (blue symbols) and 10 – 100 Hz (red symbols).*

Figure 21 shows the amplitude ratios of the fundamental mode Rayleigh waves (*Rg*) with respect to SH1 (red dots). The amplitude ratios for the *P*-waves are shown for comparison (blue dots). *Rg* amplitudes were measured as the maximum of the envelopes in the *Rg* window for stations with distances greater than 1 km showing prominent dispersive arrivals. The traces were filtered between 1 and 10 Hz. Because of the strong topographic variations in the area, some of the stations are lacking *Rg* phases and are not shown. Notice that for the majority of the events shown in Figure 21, the ratios for *P* and *Rg* amplitudes are similar on average. The only exception is the Octol shot (SG4), for which the amplitudes of the *Rg* phases are consistently lower than the ratios between the *P* waves. This observation could be explained, for instance, by the presence of a vertical dipole component added to an isotropic component.

Figure 22 shows the effect of the VOD on the seismic radiation in the low- and high-frequency bands by comparing the ANFO shot (SH5) and the Octol shot (SG4) filtered between 1 and 10 Hz (Fig. 22a,c) and between 10 and 100 Hz (Fig. 22b,d). The seismograms recorded at two stations located at approximately 6 km (RDSX and ZR02) are shown. Notice the scattered *Rg* phase for Station ZR02 because the wave has to cross a river valley to get to the station. In the low-frequency band *P*-wave amplitudes are similar between the two events, whereas the *Rg* amplitudes are higher

by a factor of 2 or more for the ANFO shot. In the high-frequency band the *Rg* phase is either very small or not visible. The *P*-wave amplitudes are comparable between the two events.

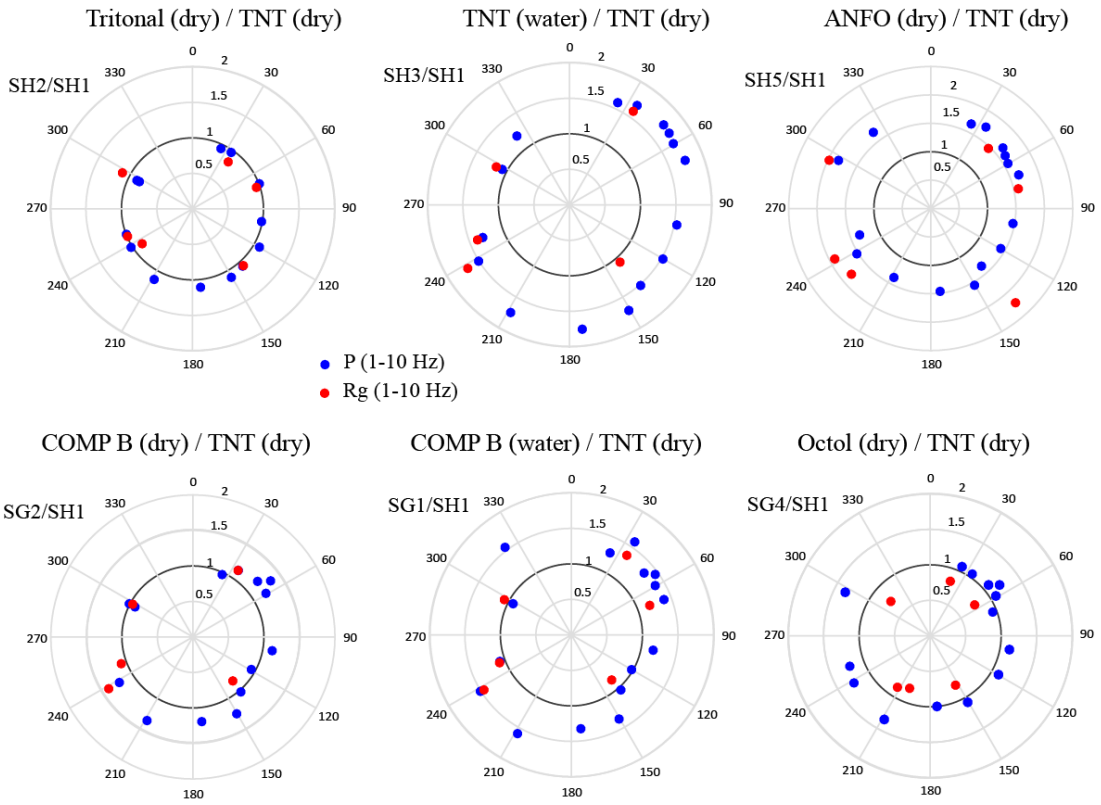

Figure 21. *P*-wave amplitude ratios plotted as a function of the station azimuths for the event pairs: (a) SH2/SH1; (b) SH3/SH1, (c) SH5/SH1, (d) SG2/SH1, (e) SG1/SH1, and (f) SG4/ SH1. *The amplitudes were extracted from the waveforms filtered between 1 – 10 Hz (blue symbols) and 10 – 100 Hz (red symbols).*

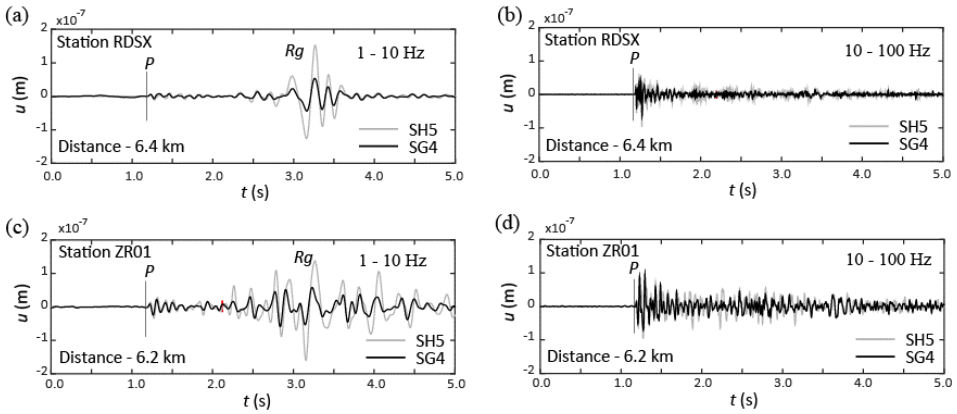

Figure 22. Vertical component displacement seismograms for SH5 (ANFO) and SG4 (Octol): (a) Station RDSX (filtered between 1–10 Hz), (b) Station RDSX (filtered 10–100 Hz), (c) Station ZR01 (filtered 1–10 Hz), (d) Station ZR01 (filtered between 10 and 100 Hz). *All seismograms are plotted to the same scale.*

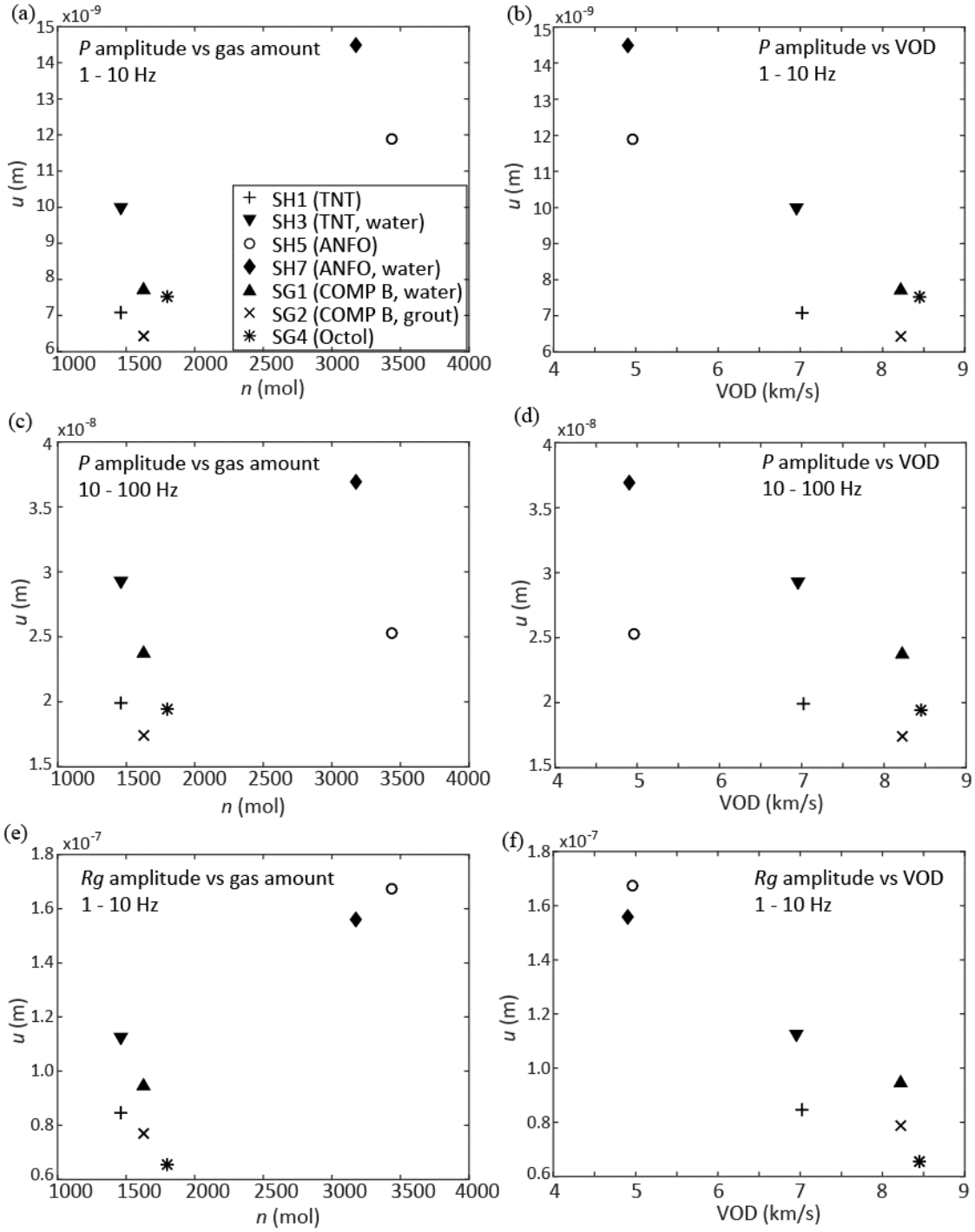

Figure 23. Vertical component amplitudes averaged over 4 short period stations (ARR2, SZAU, R115, and RDSX) for all 7 shots: (a) *P* amplitude vs the amount of gas products released by explosive charge filtered 1–10 Hz, (b) *P* amplitude (filtered 1–10 Hz) vs the explosive VOD, (c) *P* amplitude (filtered 10–100 Hz) vs the amount of gas, (d) *P* amplitude (filtered 10–100 Hz) vs VOD, (e) *Rg* amplitude (filtered 1–10 Hz) vs the amount of gas, (f) *Rg* amplitude (filtered 1–10 Hz) vs VOD.

Figure 23 shows *P* and *Rg* amplitudes measured from the waveforms filtered in the low- and high-frequency bands (1 – 10 Hz and 10 – 100 Hz respectively). The amplitudes are plotted as a function of the volume of gaseous detonation products (Fig. 23 a, c, e) and the VOD (Fig. 23 b, d, f). The increase in the gas volume results in an increase in seismic amplitudes for both *P* and *Rg* phases, whereas the increase in the VOD results in a decrease in seismic amplitudes. Interestingly, the *P* amplitudes appear to be affected by water present in the borehole during the detonation (solid symbols), whereas the *Rg* amplitudes do not appear to change significantly for the shots in the water-filled boreholes. Overall, the *Rg* amplitudes show the most pronounced downward trend with the increase in the VOD.

4.3. Relative Moment Tensor Inversion

The relative moment tensor inversion (RMTI) method was developed during our previous GAS2016 (under contract FA9453-16-C-0021) in order to determine the MT from explosions and other shallow events recorded at local to near-regional distances. The method is similar to the technique developed by Dahm (1996) for the body waves. The technique used in this study incorporates the fundamental mode Rayleigh waves (*Rg*), which have large amplitudes for shallow events. In Stroujkova (2018b) the method was used to calculate the MTs for the 6 explosions conducted in 2016. In this report, we used this approach for all 10 explosions of the combined dataset.

Table 4. MTs calculated for the combined dataset using SH1 as a reference.

Shot	M_0*	M_{xx}	M_{yy}	M_{zz}	M_{xy}	M_{xz}	M_{yz}	M_{ISO}	M_{CLVD}	M_{DC}	K
SH1	1.00	1.00	1.00	1.00	-0.01	0.00	0.00	0.99	0.01	0.00	1.01
SH2	0.99	0.98	1.01	0.99	-0.07	-0.12	0.01	0.87	0.01	0.12	1.00
SH3	1.53	1.05	0.85	1.05	0.16	-0.11	0.07	0.79	0.11	0.10	1.11
SH5	1.66	1.00	1.12	0.84	-0.07	0.04	-0.10	0.83	0.03	0.14	0.80
SH6	2.59	0.91	1.14	0.91	0.03	0.04	-0.17	0.80	0.09	0.11	0.89
SH7	1.90	0.98	0.93	1.06	0.14	-0.01	-0.05	0.85	0.08	0.07	1.11
SG1	1.38	0.98	0.87	1.09	0.13	0.02	-0.17	0.79	0.08	0.13	1.19
SG2	1.14	0.84	1.00	1.11	0.23	-0.14	-0.07	0.75	0.03	0.22	1.23
SG3	1.42	0.84	1.00	1.12	0.09	-0.02	-0.01	0.84	0.08	0.08	1.22
SG4	1.11	0.80	0.92	1.23	0.03	0.04	-0.03	0.79	0.11	0.10	1.44

* The scalar moments are calculated with respect to the reference events.

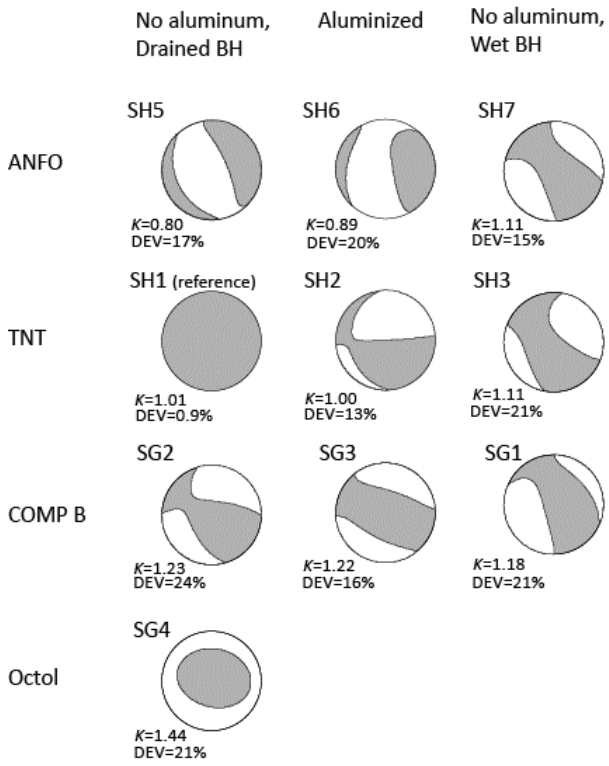

Figure 24. Deviatoric MTs for the events of the dataset using events SH1 as a reference.

The RMTI was constrained by using SH1 sources as reference mechanisms. The reference MTs are set to purely isotropic mechanisms. Past studies (e.g. Stroujkova et al, 2012; Stroujkova et al, 2015; Stroujkova, 2018b) show that explosives with high velocity of detonation and low gas content (e.g. TNT) tend to produce a higher percentage of isotropic component. Therefore, Shot SH1 (TNT shot in the drained borehole) was used as a reference mechanism.

Figure 24 shows the deviatoric parts of the MTs for each event of the dataset. Notice the progression of the principal extension axes from near-horizontal for ANFO-based explosives to near-vertical for Octol. Table 4 shows the results of the MT inversion, including the individual scalar moments, MT components and the values of parameter *K* introduced by Patton and Taylor (2008) to quantify a measure of the relative strengths of the vertical and the horizontal dipoles:

$$K = \frac{2M_{zz}}{M_{xx}+M_{yy}}. \quad (1)$$

As shown in Table 4, the parameter *K* reaches its highest value for the Octol shot (SG4) and the lowest for the ANFO shot (SH5). Figure 25 shows *K* plotted with respect to the VOD of the explosives. The error bars were calculated using the jackknife estimation technique. Notice an increase in *K* with the increase in the VOD. To test the robustness of this result, we calculated the MTs using SH2 as a reference event as was done in Stroujkova (2018b). These values, plotted as grey symbols in Figure 25, are within the error bars for all of the events and follow the same trend.

This example shows that the effect of the VOD on the value of parameter K is independent of the choice of the reference event.

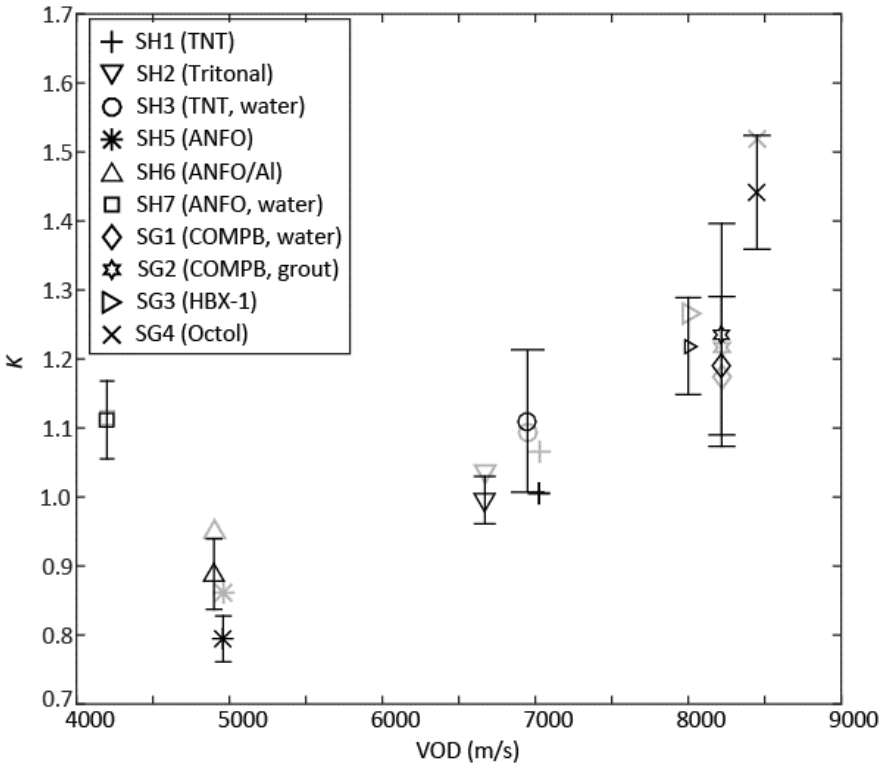

Figure 25. Parameter *K* plotted as a function of the VOD. ***Black and grey symbols show K calculated using the results of the RMTI using the reference events SH1 and SH2 respectively. The error bars were obtained using the jackknife estimate performed by leaving each measurement out.***

4.4. Conclusions

The results of the experiment confirmed *P* and *Rg* amplitude reduction as a function of the explosive VOD, particularly in the low-frequency band (1 – 10 Hz). High gas content, low VOD explosives result in higher non-isotropic component. The increase in non-isotropic component correlates with larger fractures produced by these explosions. It is important to point out that the explosives with low VOD often release higher amounts of gaseous products. For instance, ANFO has the lowest VOD (5000 m/s) and the estimated amount of gas is 43 moles per 1 kg of TNT equivalent, compared to only 25 moles per 1 kg for the TNT. Not only are the amplitudes larger for low-VOD high-gas explosives, but also the amplitude increase is non-uniform in different directions, which indicates differences in the radiation patterns.

The results of the RMTI applied to the combined dataset reveal that the relative strength of the vertical dipole compared to the strength of the horizontal dipoles (index *K*) increases systematically with the increase of the VOD. This increase corresponds to the decrease in the *Rg* amplitudes with respect to *P* amplitudes. Patton and Taylor (2011) proposed an explosion model,

which explains weaker surface waves by a superposition of an isotropic component and a vertical CLVD attributed to a shock-induced extensional deformation along the vertical axis accompanied by medium damage. Our new results, using explosives with a wide range of the VOD, support the increase in vertical dipole for the explosions resulting in crater formation.

5. YIELD ESTIMATE USING SURFACE WAVES

Anastasia Stroujkova, Vanessa Napoli

5.1. Introduction

It was shown in the previous section that seismic amplitudes vary significantly between the events of nearly the same yield depending on the explosive type and the emplacement conditions (e.g. water in the shot borehole). For instance, the *Rg* amplitudes decrease as the velocity of detonation increases. *Additionally, differences in the seismic amplitudes, due to the differences in the explosive type, result in the discrepancies in the seismic yield estimate.* In this section we examine the effect of the explosive type on the yield estimate using the fundamental mode Rayleigh waves (M_{Rg}, e.g. Bonner and Russell, 2013).

5.2. MRg yield estimate

In order to quantify the effect of the explosion type on the amplitude, we estimated the yield using the M_{Rg} method proposed by Bonner and Russell (2013) and further developed in Napoli and Russell (2018). The details of the magnitude (M_{Rg}) and the yield estimation are given in Bonner and Russell (2013) and Napoli and Russell (2018). For the laterally homogeneous or slowly changing velocity structure, the magnitude is defined as:

$$M_{Rg} = \log_{10} u + 0.5 \log_{10} r - \log_{10} f_c + 0.4343\gamma r + E(f) - 2.36, \quad (2)$$

where

$$f_c = \frac{10.54 f g_{min}}{\sqrt{r}} \ . \quad (3)$$

In Equation 2, *u* represents the observed displacement, *r* is the source/receiver distance, and γ is the attenuation correction. The second term in Equation 2 represents the geometric spreading correction, the third term corrects for narrow-band filter widths (Russell, 2006), the fourth term implements the attenuation correction, and the fifth term is so-called source excitation term (Bonner and Russell, 2013) correcting for the ratio of short-period to long-period (20s) surface waves. It was shown previously (e.g. Napoli and Russell, 2018) that the yields estimated using this technique are generally within 20% of actual.

Assuming power law scaling between seismic amplitudes and yield; the magnitudes, including M_{Rg}, have a linear relationship with the logarithm of the yield:

$$M_{Rg} = a + b \log_{10} Y \quad (4)$$

To calculate the coefficients *a* and *b*, a suite of synthetic waveforms for a range of yields (1kg – 1kt) was calculated. The attenuation for the surface waves was calculated from the observed

data. The averaged Q was calculated from the network data using the observed peak Rg amplitudes narrowband filtered around 3Hz. The source moment (M_0), needed to compute the synthetic waveforms for a given yield, was calculated using Denny and Johnson (1991) source scaling with the following relationship (e.g. Ford and Walter, 2013):

$$M_0 = Y\left[4.2743X10^{10}\ V_p^2\ V_s^{-1.1544}\ P_0^{-0.4385}\ 10^{-0.0344GP}\rho\right], \quad (5)$$

where V_p and V_s are the seismic velocities, P_0 is the overburden pressure, GP is the gas-filled porosity at the source (0.5% for the granite), and ρ is the density. The synthetic seismograms were calculated using Computer Programs in Seismology Version 3.30 (Herrmann, 2013).

Table 5. Yields estimated using MRg

Event	Network averaged M_{Rg}	Y_{Rg} (kg TNTe)	Y_d (kg TNTe)
SH1	-0.569	82.35	63.2
SH2	-0.645	69.72	96.2
SH3	-0.536	88.39	63.2
SH5	-0.359	130	63.1
SH6	-0.15	203	94.1
SH7	-0.39	121	60.9
SG1	-0.557	84.52	63.4
SG2	-0.685	63.78	63.4
SG3	-0.496	96.48	82.6
SG4	-0.761	54.03	62.8

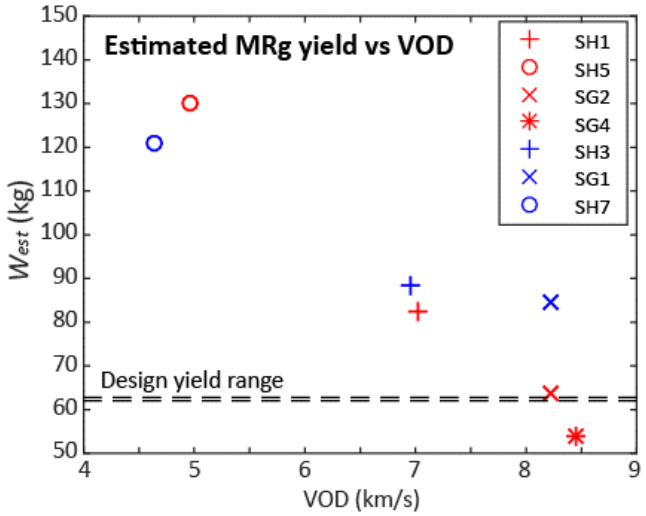

Figure 26. Estimated M_{Rg} yield plotted as a function of the explosive VOD for non-aluminized shots.

After the synthetic waveforms were calculated, the peak *Rg* amplitudes were measured from the narrow-band filtered waveforms with a central frequency of 3Hz. The amplitudes were then used to determine the coefficients *a* and *b* in Equation 4. The final formula used to estimate the yield from the *MRg* is:

$$M_{Rg} = -2.5349 + 1.0273 \log_{10} Y. \quad (6)$$

The estimated yields for each explosion of the dataset are shown in Table 5. Notice that the estimated yields vary considerably, even for the events with approximately the same design yields Y_d highlighted in Table 5. There is a consistent reduction in the estimated yield from the low VOD explosives (ANFO) and the high VOD explosives (Octol). The yield estimated for SH5 (130 kg) is higher than the yield for SG4 (54 kg) by a factor of 2.4.

5.3. Conclusions

The waveform analysis in the previous chapters shows that low-frequency (1 – 10 Hz) seismic *P* and *Rg* amplitudes decrease as the VOD increases. To quantify the differences in the seismic amplitudes we estimated the yield based on the fundamental mode Rayleigh wave (*Rg*). For the non-aluminized explosives, the estimated yields vary by a factor of 2.4, despite the fact that their design yields were different by no more than 4% (between 60.9 kg TNTe for SH7 and 63.4 kg TNTe for SG1 and SG2). The difference in the estimated yield is attributed to the source term because the propagation paths are virtually the same for each event-station pair.

6. ACOUSTIC OVERPRESSURE ANALYSIS

6.1. Introduction

We analyzed acoustic overpressure signals generated by overburied underground chemical explosions conducted in hard rock in New Hampshire in 2018. All of the explosions discussed in this article had comparable yields and were buried at depths between 12 and 13 m. Two explosions resulted in crater formation and gas venting, whereas the remaining explosions were fully confined and did not result in ground surface failure. Acoustic signals from the confined explosions are produced by the ground shock near the ground zero and can be approximated using a Rayleigh integral of the near-source ground acceleration. Acoustic signals from cratered explosions represent a combination of a ground shock signal and a time-delayed high-amplitude signal created by gas venting. The cratering/venting occurred during the free-fall phase observed on the near-source accelerograms. The impulse of the gas venting signal from the two cratered explosions is equivalent to a small surface blast of approximately 0.5–2% of the design yield of the explosions. We hypothesize that the main reason for the cratering in this experiment is the low medium porosity, preventing post-explosion pressure relief in the cavity, thus promoting long fracture formation during the unloading phase and subsequent containment failure. *The amplitudes of the acoustic signals produced by these explosions are significantly higher than expected from overburied explosions, which may potentially lead to errors in yield estimate.*

Acoustic overpressures from underground explosions depend on the depth of burial (DOB) and the degree of confinement. Previous studies have shown that the acoustic amplitudes decrease with the increase in DOB. Various empirical models have been proposed for the prediction of the acoustic overpressures as a function of the yield and the DOB (e.g. Ford et al, 2014; Bowman, 2019). For fully confined explosions the acoustic signals are generated by the ground surface displacement caused by the shock wave reaching the surface. This signal is called the ground-shock-induced (GSI) air blast (e.g. Vortman, 1962, 1970; Snell et al, 1971). The GSI pulse can be modeled using the Rayleigh integral (e.g. Jones et al, 2015).

Explosions resulting in ground failure exhibit a gas-venting-induced (GVI) pulse (e.g. Vortman, 1962; Snell et al, 1971) in addition to the GSI signal. The overpressure signals due to the gas venting depend on the volume and the gas pressure in the cavity at the time of venting. The majority of the data showing both GSI and GVI phases come from cratering (underburied) explosions (Vortman, 1970), both nuclear and chemical. Vortman (1970) states that the chemical explosions produce significantly higher GVI pulses than the nuclear explosions. It was shown in the previous studies that the GVI signals from the explosions buried deeper than approximately 60 $m/kt^{1/3}$ are significantly lower than the GSI pulses (e.g. Vortman, 1970; Snell et al, 1971).

In this report we analyze seismic and acoustic data from four overburied chemical explosions (scaled DOB greater than 2 $m/kg^{1/3}$) conducted in New Hampshire in 2018. The unique characteristic of the new dataset is that it includes both fully confined and cratered explosions conducted in the same quarry.

6.2. Acoustic Data

The explosion experiments were monitored using seismic and acoustic networks deployed from the near-source to local distances. The explosions were conducted during two separate deployments. Figure 27 a-b shows the stations used in this study. Stations shown with solid triangles were deployed both in 2016 and 2018, whereas stations shown as grey triangles were only deployed in 2016. The acoustic measurements were made using Hyperion IFS-5311 seismically-decoupled infrasound sensors with 100 Pa maximum pressure range. The acoustic sensors were fielded in a distance range between 40 m and 4 km and were covered with foldable mesh domes to reduce wind noise. The acoustic signals from the explosions were observed at all acoustic sites located between 40 m and 4 km from the explosions. The largest amplitude of 999 Pa was recorded for the cratered shot SG4 by a station located 40 m from the shot. The lowest amplitude of approximately 0.05 Pa was observed for SG3 recorded by station WARR located at a distance of 4 km from the sources. This value is close to the noise floor for WARR; therefore, we did not use this station for the data analysis.

Figure 15 shows the overpressure records from Station NE03 located at the distance of approximately 800 m from the sources. At this location fully confined shots SG1 and SG3 produced overpressures on the order of 10-20 Pa, whereas the overpressures from the vented shots were an order of magnitude higher – between 100 and 200 Pa. The signals from the cratered shots are represented by a superposition of the GSI and GVI pulses. Comparison with the fully confined shot (SG3) shows that the GSI signals are similar between the vented and the fully confined events, and the GVI pulse is delayed with respect to the lower-frequency GSI signal. The time delay is approximately 40 – 60 ms for SG2 and 120 ms for SG4.

To understand the acoustic overpressure signals, we plotted the near-source accelerometer records for the sensors located approximately 1 m from the shot boreholes (Fig. 28). The near-source records show the impulsive shock wave arrivals, followed by a period of downward acceleration (dwell) and a series of spikes resulting from slapdown(s). Shots SG1 and SG2 were conducted using identical COMP B charges, however the amplitude of the first peak for SG1 is more than twice as high as the amplitude for SG2. Shot SG1 (COMP B in a stemmed borehole containing water) produced the highest amplitude for the first arrival. Shot SG2 (grouted borehole) resulted in the ground failure and produced a crater. The near-source accelerogram from SG2 shows a complex signal starting approximately 40 ms after the first peak, which culminated with venting, ground failure and ejection of the accelerometer, which was found several meters from the initial location. Shot SG4 also resulted in the ground failure and ejection of the accelerometer. In this case, the high-amplitude signal, apparently related to the venting and ground failure, initiates at 100 ms and peaks approximately 120 ms after the first arrival. Notice that in both cases the ground failure starts long after the passage of the shock wave and, in the case of SG4, after the dwell phase. This observation shows that the cratering was produced as a result of the late time damage rather than caused by the shock wave. The signal related to the cratering from the accelerometer records appears to be shorter than from the acoustic records. The reason is that the acoustic wave is generated over a large surface area, which results in the long signal duration due to a finiteness of the source.

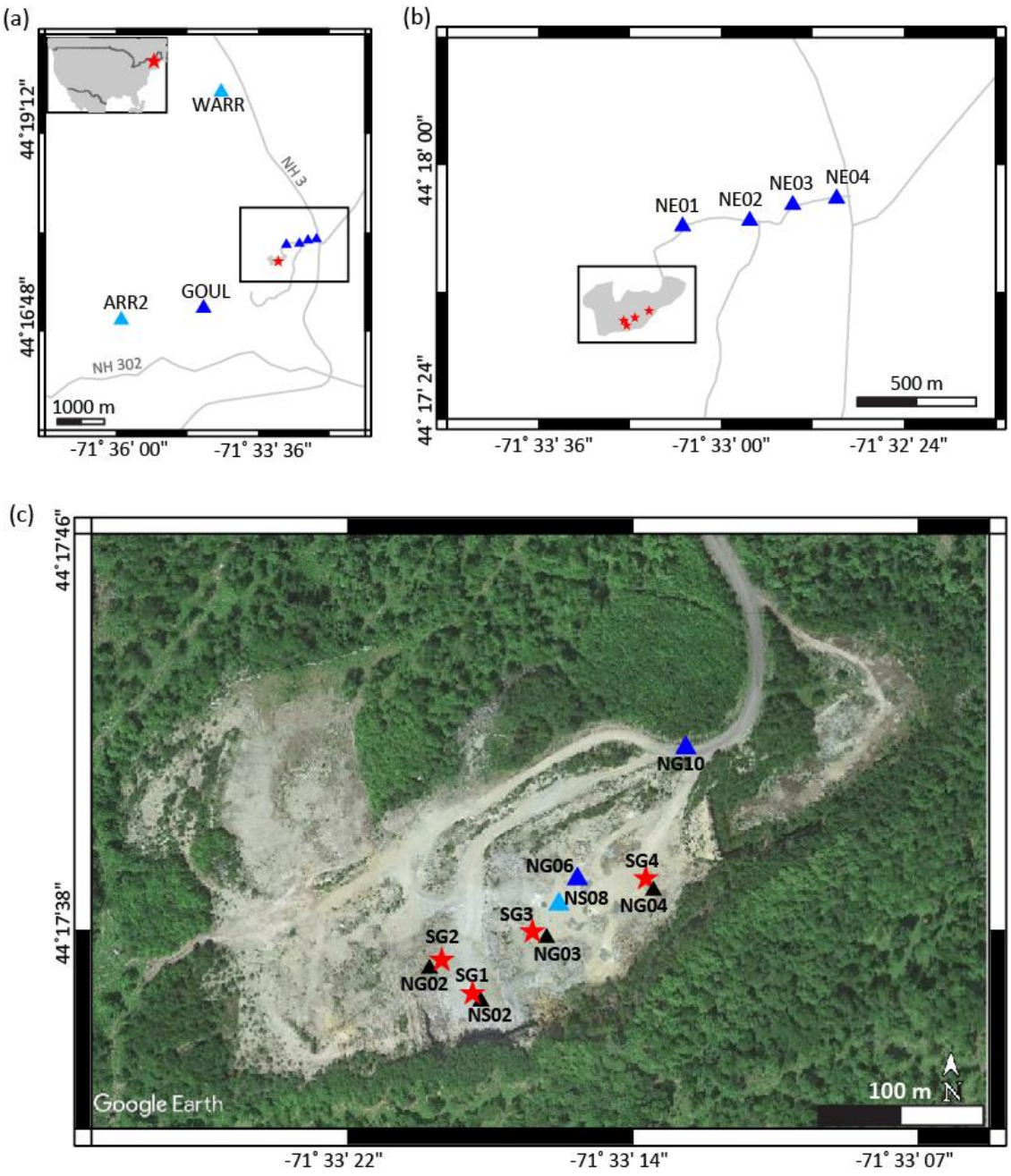

Figure 27. (a) A map of the area of Carroll, New Hampshire (USA) showing the experiment location (red star) and the acoustic stations. ***The dark blue triangles show the stations deployed during both June and October experiments; the light blue triangles show the stations deployed only in October 2018. The inset in the upper left shows the map of the continental United States and the experiment location marked as a red star.*** **(b) Enlarged view of the quarry with the stars showing the shot locations. (c) Enlarged view of the test bed.** ***The blue triangles show co-located acoustic sensors and accelerometers deployed in June (light blue) and October (dark blue). The black triangles show the locations of the ground-zero near-source accelerometers.***

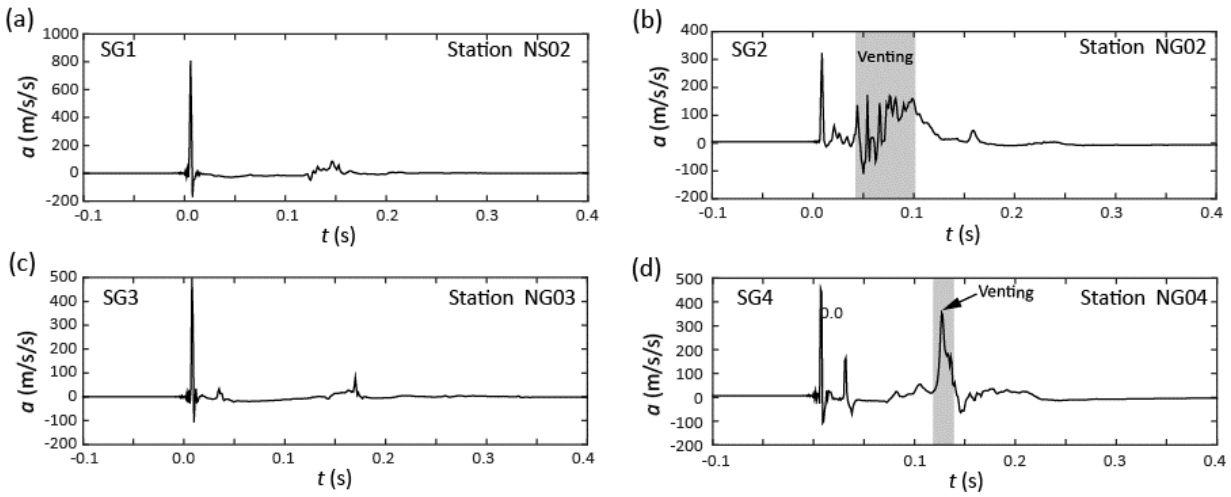

Figure 28. Near-source accelerometer records for: (a) SG1, (b) SG2, (c) SG3, (d) SG4. The accelerometers were located between 1 – 1.5 m from their respective shot boreholes.

6.3. Fully confined explosions

Two of the explosions (SG1 and SG3) did not result in a ground failure and were fully confined. For fully confined explosions, the acoustic waves are generated by the ground displacement. The Rayleigh integral can be used to estimate acoustic signals produced by underground explosions using ground acceleration (e.g. Banister, 1991; Jones et al, 2015):

$$p(x,y,z,t) = \frac{\rho_0}{2\pi R}\int_S \; a\left(x', y', t - \frac{R}{c_0}\right) dS \,, \tag{7}$$

where ρ_0 and c_0 are the ambient density and the speed of sound of the air, a is the surface acceleration in the source region, S is the source area, and x' and y' are the coordinates within the source area.

To model the surface source of acoustic waves we need to approximate the ground acceleration around the ground zero. Jones et al (2015) used a network of close-in accelerometers to interpolate for the distributed source function. Unfortunately, such a dense near-source network is not available in our case. Instead we used the source-time function from the ground zero accelerometers multiplied by a decay function in the form:

$$a_p = AR_{sl}^B \,, \tag{8}$$

where a_p is the peak acceleration, R_{sl} is the slant distance, and A and B are the fitting parameters estimated using linear regression. Figure 29a shows the relationship between the observed peak acceleration and the slant distance for shots SG1 and SG3. The slopes estimated using linear regression are -2.05 for SG1 and -2.15 for SG3. These values are in a good agreement with the free-field accelerometer data from nuclear explosions of Perret and Bass (1975) for hard rock (2.32 ± 0.08) and wet tuff (2.02 ± 0.29).

For the simulations we used the exponent $B = -2.10$. The amplitude decays rapidly at distances exceeding the DOB. In addition, the SG1 location is surrounded by the quarry walls in the south and west and there is a drop to the lower level in the east, all located approximately 15 m from the shot location. The SG3 shot also had a wall east of the shot location and large rock piles in the south, which also limits the area of the acoustic source. Therefore, the integration (Eq.7) was performed within a radius of 15 m using 0.01 m grid spacing.

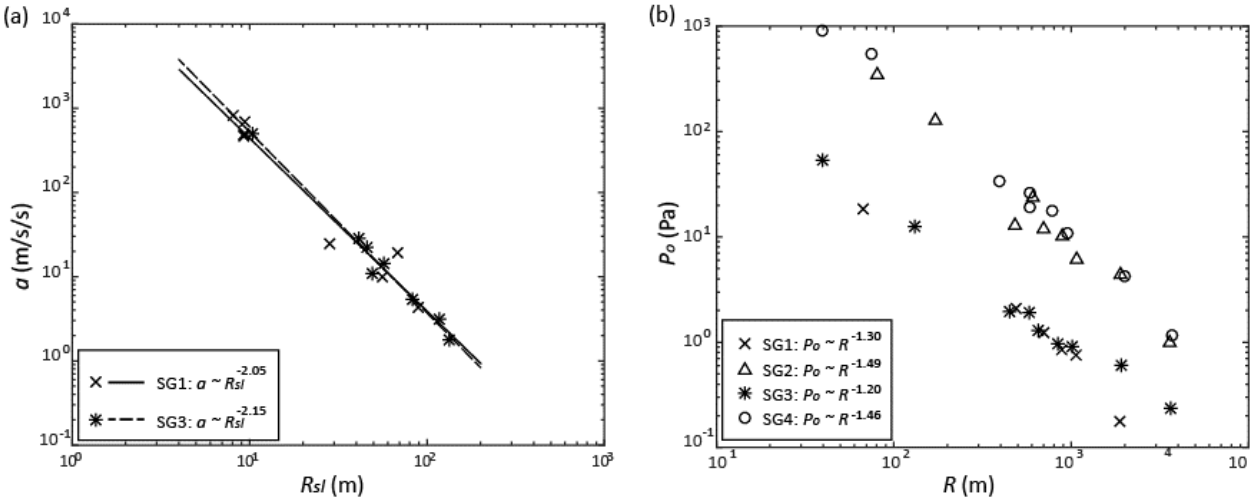

Figure 29. (a) Peak acceleration plotted as a function of the slanted distance for the near-source accelerometers for SG1 and SG3. (b) Peak overpressures plotted as a function of the stand-off distance.

Table 6. Physical characteristics of the atmospheric air during the experiment.

Parameter	June 26	October 24
T (°K)	295	273
P (kPa)	960	960
c (m/s)	344	331

The sound velocity, required for calculation of the acoustic waveforms, is temperature dependent and can be approximately estimated using the following expression:

$$c_a = 331.3 + 0.606\theta, \tag{9}$$

where θ is a temperature in °C. Shot SG1 was conducted on June 26, 2018. The temperature during the day was approximately 22°C (295°K). The elevation at the experiment site is 520 – 530 m, therefore the barometric pressure on the day of the blasting varied between 95 and 96 kPa. Using Equation 9, we estimated the sound speed on June 26 to be approximately 344.63 m/s. The

estimated sound speed measured from the first arrivals for June 26 is approximately 343.75 ± 1.19 m/s.

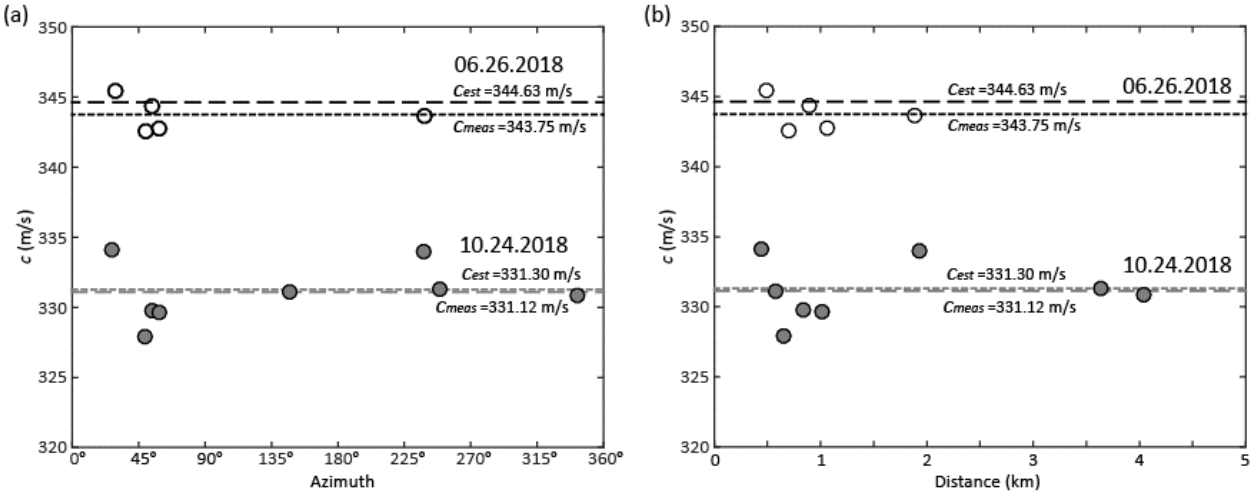

Figure 30. Sound speeds for the days of the shooting (June 26 and October 24) estimated from the travel times and temperature plotted as a function of (a) azimuth and (b) distance between the sources and receivers.

Shot SG3 was conducted on October 24, 2018, when the air temperature was approximately 0°C (273°K). The estimated sound speed for that temperature is 331.30 m/s. The measured sound speed (Fig. 30) for October is 331.6 ± 2.1 m/s.

Figure 30 a-b shows the sound speed estimated from the individual travel times as a function of azimuth and distance, respectively, compared with the theoretical speeds estimated using Equation 1. Since no wind speed observations were made and no apparent azimuthal bias was determined from the sparse data, we used a constant sound velocity for both days.

Thus, to perform the simulations the following simplifications were made: 1) radially symmetrical source region with peak acceleration decay inversely proportional to the distance squared, 2) constant sound velocity with no wind, and 3) complex topography was not considered. The synthetic waveforms are shown in Figure 31. Note that no amplitude normalization, filtering or time shift were applied to the synthetic data to improve the visual waveform match. The overall amplitudes and the shapes of the impulses are matched, however there are additional complexities of the waveforms that could not be reproduced due to a very simple model. The phases following the second peak are possibly caused by reflections off the quarry walls. This example shows that the Rayleigh integral can produce reasonably realistic results using a very simple model.

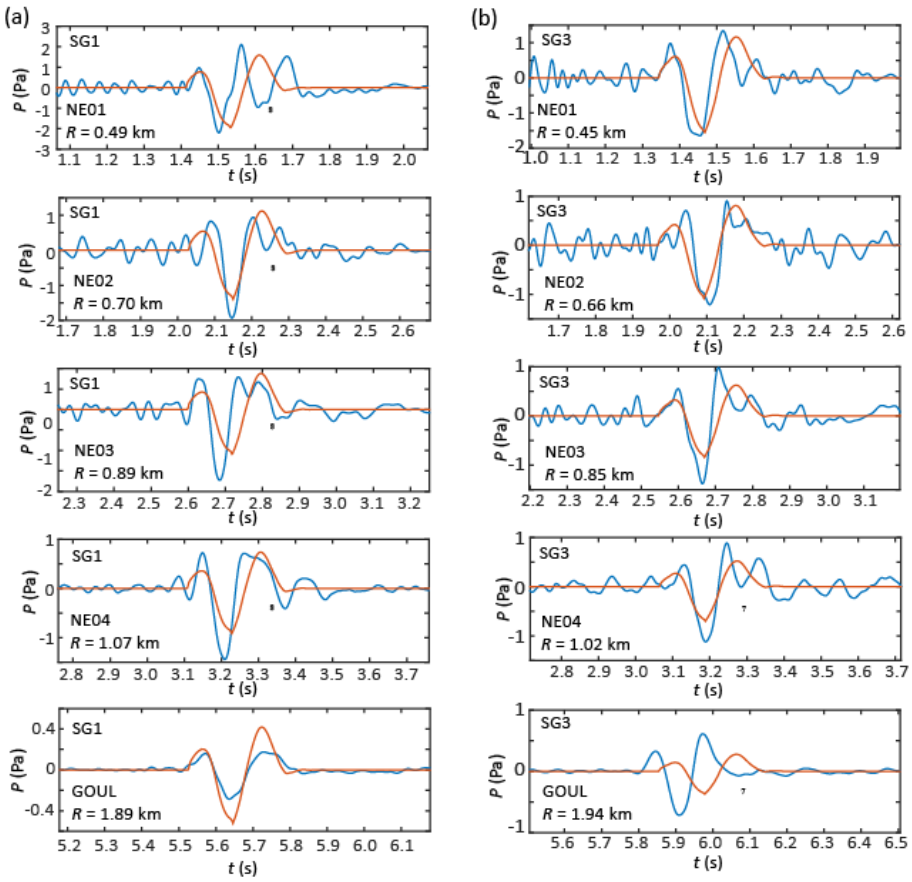

Figure 31. Comparison between the data and the synthetics calculated using the RI. (a) Shot SG1, and (b) Shot SG3.

6.4. Cratered explosions

Events SG2 and SG4 resulted in ground failure and ejection of near-surface rocks due to venting of the pressurized cavity gas. The venting can be modeled as a gas flow from the cavity through an open pathway (e.g. a fracture or a borehole) created by the blast. Figure 32 shows the acoustic overpressures recorded by the near-source station NG06. Shot SG2, located at a distance of 80 m from NS06, produced a peak amplitude of 354 Pa. The peak amplitude of the GVI signal for Shot SG4 recorded at a distance of 39 m (Station NS06) is 999 Pa. Figure 33 shows the acoustic waveforms for SG2 and SG4 compared with the fully confined shot SG3. The time delay between the detonation and the venting on the order of tens of milliseconds indicates that the pathway opens after the wave reaches the free surface during the unloading phase. By that time a considerable portion of the total explosion energy is lost due to gas expansion resulting in the cavity formation. In addition, some of the energy is lost to heat exchange with the medium.

The waveforms of the high-amplitude acoustic waves change as they propagate because higher amplitudes travel faster than lower amplitudes. As a result, an impulse of any shape would eventually develop a shock discontinuity if there was no dissipation. The distance the wave needs to travel to transform into a shock depends on the initial amplitude and a dominant period of the

signal. We can use a weak shock model in a lossless atmosphere (e.g. Blackstock et al, 1998) to approximately determine the source parameters of the vent. The source of the acoustic waves can be described by gas flow through a borehole with a diameter of 25 cm ($r_0 = 0.125$ m). A spherical sinusoidal wave with a peak overpressure of p_0 would break (form a shock discontinuity) at a distance r_s calculated as follows (e.g. Blackstock et al, 1998; Naugolnykh and Ostrovsky, 1998):

$$r_s = r_0 \, exp\left(\frac{c_0^2}{r_0 \epsilon \omega u_0}\right), \tag{10}$$

where u_0 is the particle velocity at the source, $r_0 = 0.125$ m is the source radius (assuming that the venting occurred through the opening close in diameter to a borehole), c_0 is the acoustic velocity of air, ω is the wave period, and for the wave in the air ($\gamma \approx 1.4$) and

$$\epsilon = \frac{\gamma+1}{2} \approx 1.2. \tag{11}$$

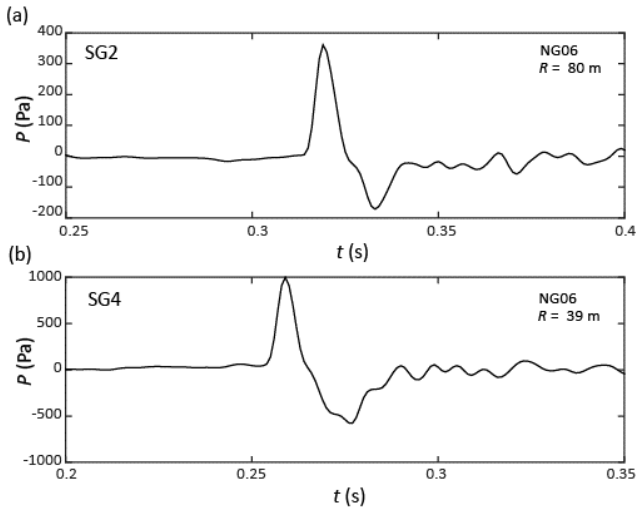

Figure 32. Acoustic overpressures for the vented events recorded by the near-source station NG06: (a) SG2 and (b) SG4.

In our case, both SG2 and SG4 produced a signal with a positive phase duration of approximately 11 ms and a rise time of 5 ms without sharp discontinuities. Using the positive phase duration of approximately 11 ms as a half wavelength ($\lambda/2 = 0.011\ s$) the signal dominant frequency is $f = 45$ Hz. Using Equation 10 we estimate that such impulse with an initial overpressure $P_0 = 410$ kPa would break at a distance of 40 m. The signal from Shot SG4 did not break at 40 m; therefore, we conclude that the source amplitude should not exceed 410 kPa in the absence of dissipation.

The overburden pressure at the cavity depth ($h \approx 10$ m, Figure 19) is $P_c = \rho_r g h = 255$ kPa, where $\rho_r = 2600$ kg/m^3 is the rock density. The explosion source model predicts the static cavity pressure is on the order of 1.5 times the overburden pressure; therefore, the rough estimate of the overpressure created by venting of the cavity gas $P_0 = P_c - P_{atm}$ has roughly the same order of magnitude as the upper limit for the observed signal and does not exceed the upper limit.

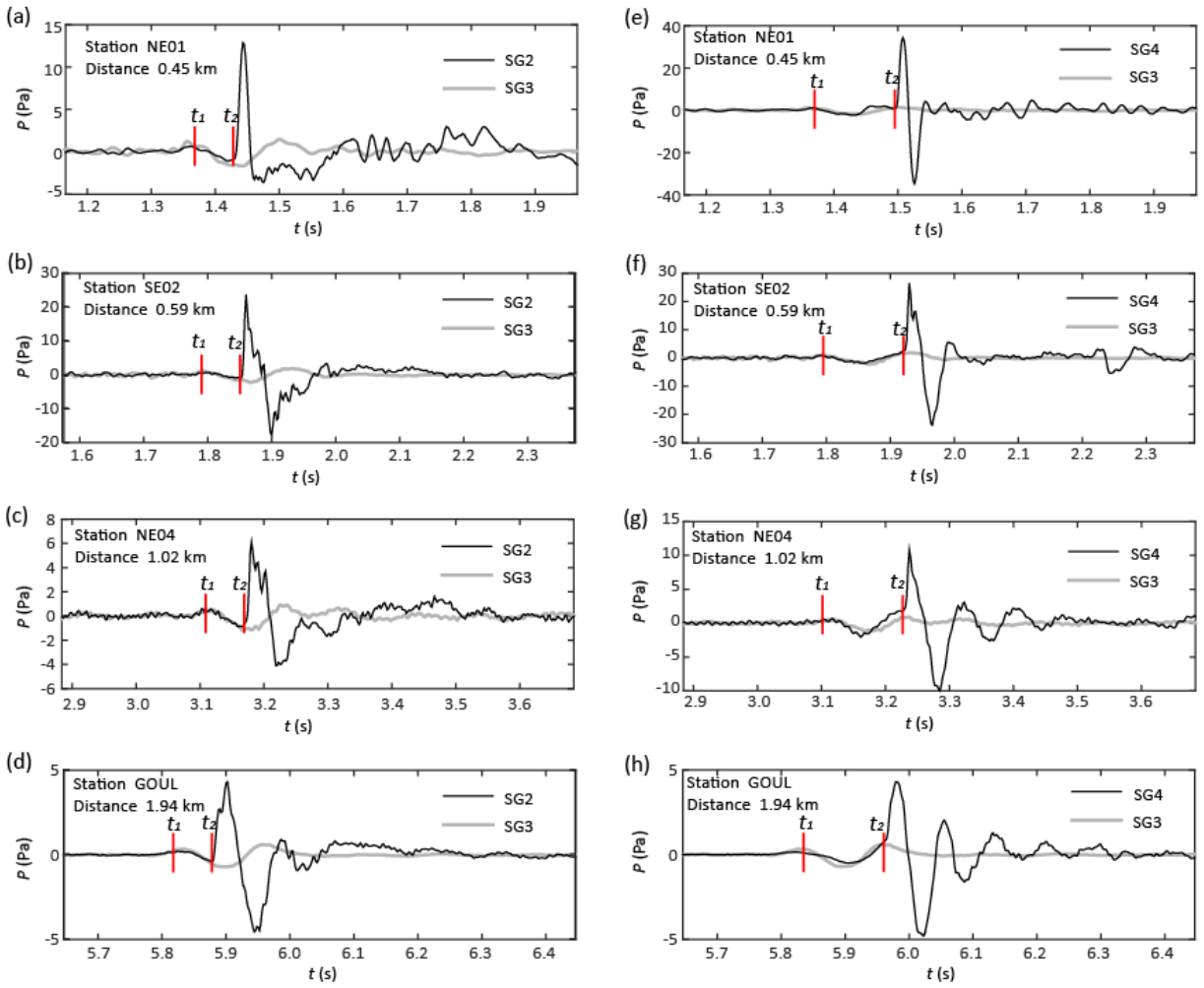

Figure 33. Acoustic overpressures for the vented events SG2 (left column) and SG4 (right column) shown with black lines compared to a fully-confined shot (SG3, grey lines): (a) SG2 recorded by Station NE01, (b) SG2 recorded by Station SE02, (c) SG2 recorded by Station NE04, (d) SG2 recorded by Station GOUL, (e) SG4 recorded by Station NE01, (f) SG4 recorded by Station SE02, (g) SG4 recorded by Station NE04, (h) SG4 recorded by Station GOUL. The arrivals of the ground-motion-related phase and the venting-related phases are marked as t_1 and t_2 respectively. *Notice, that for each station the gray lines represent the same waveform plotted to different scales.*

To estimate an approximate energy release by the cratering event, we find an equivalent surface blast using the Kinney and Graham (1985) blast model (hereafter KG85). KG85 assumes blast wave self-similarity, which implies that near-source wave characteristics are fully determined by the scaled distance to the source. For an explosion of yield W, the scaled distance Z is given by:

$$Z = \frac{R}{W^{1/3}}, \tag{12}$$

where R is the distance between the source and the sensor. Thus, the yield of the blast can be estimated from the peak overpressure, the impulse of the positive phase, or from the positive phase duration. Previous studies (e.g. Koper et al, 2002; Golden et al, 2012; Ford et al, 2014) have shown that impulse per unit area provides a more robust estimate of the yield than the peak overpressure, even outside of hydrodynamic zone. Thus, we use the impulse per unit area to determine the equivalent yield of the venting.

The impulse per unit area (I/A) is defined as the area under the pressure-time curve for the first positive phase. The scaled distance can be determined from the impulse per unit area using the following empirical relationship (Kinney and Graham, 1985):

$$I/A = \frac{0.067\sqrt{1+\left(\frac{Z}{0.23}\right)^4}}{Z^2\left[1+\left(\frac{Z}{1.55}\right)^3\right]^{1/3}}, \tag{13}$$

The scaled distance is obtained by finding the roots of Equation 13 and then converting to yield using Equation 12.

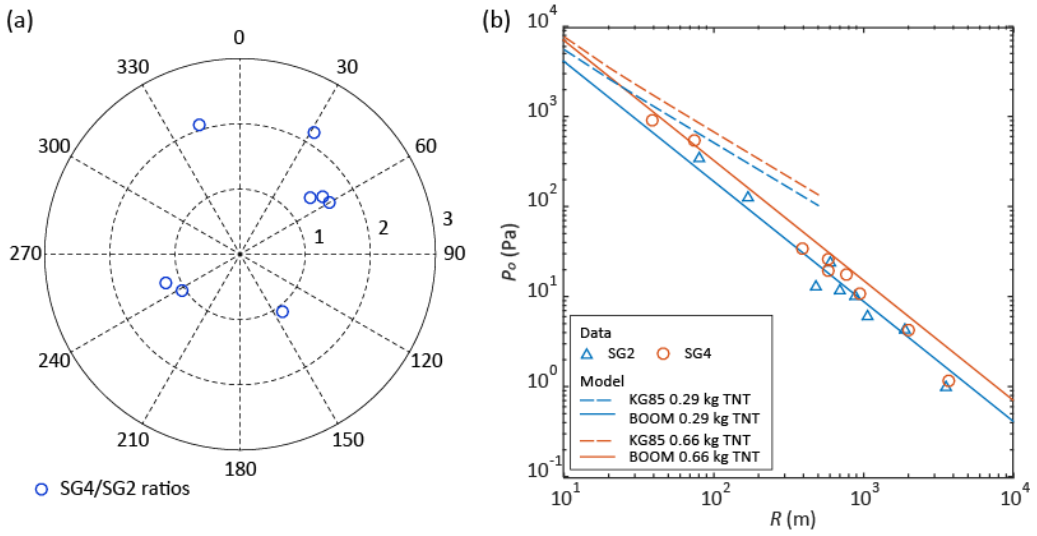

Figure 34. (a) Ratios of the peak overpressures between SG4 and SG2 for each available station with a distance greater than 400 m. *The amplitudes were multiplied by the station-event distance to correct for the location difference between the shots.* (b) Peak overpressures for SG2 and SG4 plotted as a function of the distance. Also shown are the theoretical predictions for the BOOM model and Kinney and Graham (1985; KG85) using the effective yields estimated for SG2 (W_{eff} = 0.29 kg TNT) and SG4 SG2 (W_{eff} = 0.66 kg TNT).

The peak pressure recorded for shot SG4 at a distance of 39 m was 999 Pa, which corresponds to a shock front Mach number of 1.004. The impulse estimated for SG4 at Station NG06 is 5.465 Pa-s, which corresponds to a scaled distance of 36 m/kg$^{1/3}$. Using this scaled distance, we can estimate the yield of an equivalent free-air explosion of 1.32 kg TNTe, which corresponds to the yield of a surface explosion of half that size (W^I_{eff} = 0.66 kg TNTe). The impulse estimated for SG2 is

2.047 Pa-s, which corresponds to a scaled distance of 96 m/kg$^{1/3}$ and the equivalent yield of 0.58 kg TNTe ($W^I_{eff} = 0.29$ kg TNTe for a surface explosion).

For the scaled distance of 36 m/kg$^{1/3}$ (corresponding to shot SG4 observed at NG06 at a distance of 40 m) KG85 predicts a positive phase duration of 4.13 ms and peak pressure of 2400 Pa, whereas the observed values are 11 ms and 999 Pa respectively. For shot SG2 recorded at NG06 (distance of 80 m) the estimated scaled distance is 96 m/kg$^{1/3}$, which corresponds to a predicted positive phase duration of 4.2 ms and peak pressure of 800 Pa. The observed values are 12 ms and 354 Pa. Thus, the observed near-source signals have significantly lower peak pressures and longer durations than the theoretical blast waveforms. This observation suggests that the venting source signal has longer duration and lower initial pressure than an explosive blast source function of an equivalent impulse. Note that the intention of this analysis was to find the yield of an equivalent impulse surface blast rather than estimate the energy released through the venting.

Thus, based on the near-source data, the energy released during venting for SG4 corresponds to approximately 1% of the design yield of the explosive charge. The estimated energy released by SG2 is less than half of the energy released by SG4, corresponding to <0.5% of the explosion yield. The amplitude ratio between SG4 and SG2 averaged over all far-field stations is 1.65 ± 0.56. Adjusting the amplitudes for geometrical spreading by multiplying by the station-event distances results in an amplitude ratio of 1.52 ± 0.43. These ratios are consistent with the approximate estimated yield ratio of 2. Figure 34a shows the azimuthal plot of the amplitude ratios. The directivity in the azimuthal plot indicates the presence of a non-monopole component for one or both events (possibly non-vertical gas flow through the vent).

Table 7. Yield estimate using the acoustic amplitudes and impulse per unit area.

Shot	Time delay $(t_2 - t_1)$ (s)	Station NG06				
		P_0 (Pa)	R (m)	I/A (Pa-s)	Z^I (m/kt$^{1/3}$)	W^I_{eff} (kg)
SG2	0.091 ± 0.009	354	80	2.008	80	0.58
SG4	0.167 ± 0.009	999	39	5.299	37	1.32

To validate the estimate made using the near-source data, we compared the observed far-field amplitudes with model prediction for the Blast Operational Overpressure Model (BOOM; Lorenz, 1981) given by:

$$P_{BOOM}(dB) = 103.1 + \frac{B}{5.3} + 20\, log_{10}\left[\left(\frac{p}{1013}\right)^{0.556}\left(\frac{W}{110}\right)^{0.444}\left(\frac{25}{R}\right)^{1.333}\right], \quad (13)$$
$$P_{BOOM}(Pa) = 2 \times 10^{-5}\, 10^{P_{BOOM}(dB)/20},$$

where $P_{BOOM}(dB)$ is overpressure in dB, $P_{BOOM}(Pa)$ is the overpressure in Pa, W is the TNT equivalent yield in kg, R is the range in km and B is an empirical constant (for a uniform atmosphere with no wind $B = 0$).

Figure 34b shows a comparison between measured peak overpressures for SG2 and SG4 with the theoretical predictions using the BOOM model. The KG85 model predictions are also shown for comparison. Note that the KG85 predictions were made using the yield values estimated using the impulses rather than peak overpressures. The amplitudes in the hydrodynamic zone are overestimated if W_{eff}^{I} are used. However, the amplitudes in the acoustic zone (beyond 100 m/kg$^{1/3}$) are in a good agreement with BOOM model developed for the acoustic distance range.

6.5. Conclusions

We analyzed acoustic overpressures generated by four overburied underground chemical explosions conducted in New Hampshire in 2018. Two of the explosions were fully confined and the other two resulted in ground failure and produced craters. The signals from the fully confined explosions were generated by the ground displacement at ground zero (GSI). The signals from the vented/cratered explosions represent superposition of the GSI pulse and the pulse generated by the gas venting (GVI). The GVI signals were delayed with respect to the GSI signals. Based on the analysis of the near-source accelerometer data, the venting occurred during or toward the end of the ballistic phases during the downward ground motion. The analysis of the acoustic waveforms suggests that the venting source signal has longer duration and lower initial pressure than an explosive blast source function of an equivalent impulse. We estimated the venting pressure at approximately 410 kPa and a duration of 10 – 12 ms. Studies of the acoustic waves from unconfined explosions may provide constraints on the conditions in the cavity during explosions.

Our observations show that the amplitude for the GVI pulse exceeds the amplitudes for the GSI phases by approximately an order of magnitude. Previous studies involving both chemical and nuclear explosions (e.g. Snell et al, 1971; Vortman, 1962, 1970) show that for explosions buried at confinement depths (greater than 100 m/kt$^{1/3}$ or 1 m/kg$^{1/3}$) the GVI pulse amplitudes are always lower than the GSI amplitudes. The previous observations, however, were made in relatively high-porosity rocks (alluvium, tuff, basalt, or rhyolite). The explosions discussed in this article were conducted in low-porosity granite. The common thread between the crater-producing explosions are the high VOD explosives (COMP B and Octol) and lack of permeable fractures in the emplacement boreholes. The low permeability of the emplacement medium is inferred from the fact that both boreholes were drained before the shots. We were unable to drain the boreholes with permeable fractures. Other explosions conducted in the same quarry in 2016 (e.g. Stroujkova et al, 2018a) were detonated in both drained and water-filled boreholes and did not crater. However, the 2016 explosions were conducted using explosives with slower VOD (TNT and ANFO). This observation suggests that the high loading rate caused by the high VOD explosives, in combination with lower permeability of the emplacement medium, results in high cavity pressure because the gaseous products do not have pathways to escape the cavity during the early stages. This high cavity pressure may have contributed to the containment failure during the unloading phase.

Thus, the experiment results suggest that underground explosions conducted in low-porosity rocks may result in ground failure and gas venting with higher than expected acoustic signals. Therefore, it is important to differentiate between the GSI and GVI for the purposes of the yield estimate.

7. CONCLUSIONS AND RECOMMENDATIONS

The explosion experiment (GAS2018) was a follow-up study for the GAS2016 experiment conducted in Twin Mountain, NH in 2016. The original 2016 experiment was intended to investigate the seismic signatures of the different explosive types (TNT, Tritonal, ANFO, and aluminized ANFO) in dry and water-saturated rocks. The goal of the new experiment was to further address the differences between the explosives with different VOD and the gaseous product volume.

The results of the GAS2016 experiment demonstrated that the amount of explosive gas and/ or water present in the cavity during the detonation improves seismic coupling and results in higher seismic amplitudes, particularly in the low-frequency range. The observations show that low-frequency (1 – 10 Hz) seismic *P* and *Rg* amplitudes decrease as the VOD increases. High-frequency (10 – 100 Hz) *P*-wave amplitudes also show similar trends, but to a lesser degree. The amplitude increase is non-uniform in different directions, which indicates differences in the radiation patterns. It is important to point out that the explosives with low VOD often release higher amounts of gaseous products, therefore it is difficult to differentiate between the effects of the VOD and gas content.

The new experiment revealed additional features resulting from the increased VODs of the explosives. For instance, the RMTI performed for the combined dataset reveals that the relative strength of the vertical dipole compared to the strength of the horizontal dipoles (index *K*) increases systematically with the increase of the VOD. This increase corresponds to the decrease in the *Rg* amplitudes with respect to *P* amplitudes. In addition, we observe that containment failure resulted from high-VOD detonations in the boreholes with low fracture porosity. These high-VOD explosions also show higher *K* values corresponding to an increase in a vertical dipole component. This result agrees with the Patton and Taylor (2008, 2011) model.

The differences in the explosive characteristics result in seismic amplitude variability between the types, which may cause errors in a seismic yield estimate. In our study, the yields estimated using *Rg* magnitudes (M_{Rg}) show a factor of 2.4 difference in the yield estimate for the chemical explosions of similar yields.

The acoustic observations show that the overpressure signals generated by vented/cratered explosions are an order of magnitude higher than the amplitudes produced by fully confined explosions of similar yield and DOB. The amplitudes of the acoustic signals produced by these explosions are significantly higher than expected from overburied explosions, which may potentially lead to errors in yield estimate.

Future work includes incorporating shear waves from shallow events into the RMTI, as well as evaluating various weighting schemes and constraint applications. In addition, it would be interesting to conduct similar experiments in different rock types. The effects of the VOD and the volume of the detonation products on seismic radiation may vary depending on the rock porosity, shear strength, and other characteristics.

REFERENCES

Akhavan, J., The chemistry of explosives, Royal Society of Chemistry, TJ International Ltd, Padstow, Cornwall, UK, 2004.

Ashby, M. F. and C. G. Sammis, "The damage mechanics of brittle solids in compression," *Pure and Applied Geophysics, 133*(3), pp. 489–521, 1990.

Banister, J. R. and W. V. Hereford, "Observed high-altitude pressure waves from an underground and a surface explosion," *J. Geophys. Res*., **96**, D3, pp. 5185–5193, 1991.

Bennett, D., C. Wittkop, and C. Dicken, "Bedrock Geologic Map of New Hampshire - A Digital Representation of the Lyons and others 1997 map and ancillary files," USGS Data Series 215, scale 1:250,000, CD-ROM, http://pubs.er.usgs.gov/publication/ds215,last accessed November 2017, 2006.

Blackstock, D.T., M. F. Hamilton, and A. D. Pierce, "Progressive waves in lossless and lossy fluids," in *Nonlinear Acoustics*, edited by M. F. Hamilton and D. T. Blackstock, Acoustical Society of America, San Diego, pp 65-150, 1998.

Bonner J.L. and D. R. Russell, "MRg: A Magnitude Scale for 1s Rayleigh Waves at Local Distances with Focus on Yield Estimation," *Bull. Seism. Soc. Am.,* **103**, 5, pp. 2898-2905, 2013.

Bowman, D., "Yield and Emplacement Depth Effects on Acoustic Signals from Buried Explosions in Hard Rock," *Bull. Seism. Soc. Am.*, **109**, 3, pp. 944–958, doi: 10.1785/0120180285, 2019.

Dahm, T., "Relative moment tensor inversion based on ray theory: theory and synthetic tests," *Geoph. J. Int.*, **124**, pp. 245–257, 1996.

Denny, M.D. and L.R. Johnson, "The explosion seismic source function: models and scaling laws reviewed," In *Explosion Source Phenomenology, Am. Geophys. Monograph*, **65**, pp. 1–24, 1991.

Golden, P., P. Negraru, and J. Howard, *Infrasound studies for yield estimation of HE explosions*, AFRL-RV-PS-TR-2012-0084, Air Force Research Laboratory, Kirtland AFB, NM, 2012.

Ford, S. and W. Walter, "An Explosion Model Comparison with Insights from the Source Physics Experiments," *Bull. Seism. Soc. Am.*, **103**, 5, pp. 2937–2945, doi: 10.1785/0120130035, 2013.

Ford, S. R., A. J. Rodgers, H. Xu, D. C. Templeton, P. Harben, W. Foxall, and R. E. Reinke, "Partitioning of seismoacoustic energy and estimationofyieldandheight-of-burst/depth-of-burialfornear-surface explosions," *Bull. Seismol. Soc. Am.*, **104**, 2, pp. 608–623, 2014.

Herrmann, R. B., "Computer programs in seismology: An evolving tool for instruction and research," *Seismol. Res. Lett.*, **84**, pp. 1081–1088, 2013.

Jones, K. R., R. W. Whitaker, and S. J. Arrowsmith, "Modeling infrasound signal generation from two underground explosions at the Source Physics Experiment using the Rayleigh integral," *Geoph. J. Int*. 200, pp. 779–790, 2015.

Kinney, G.F. and K.J. Graham, Explosive shocks in air, 2nd ed., Springer Science, New York, 1985.

Koper, K.D., T. C. Wallace, R.E. Reinke, and J.A. Leverette, "Empirical Scaling Laws for Truck Bomb Explosions Based on Seismic and Acoustic Data," *Bull. Seism. Soc. Am*., **92**, 2, pp. 527–542, 2002.

Lorenz, R., *Noise abatement investigation for the Bloodsworth Island Target Range: Description of the test program and New Long Range Airblast Overpressure Prediction Method*, AD-A-22292/6, Naval Surface Weapons Center, Silver Springs, MD, 1981.

Lyons, J.B., W. A. Bothner, R. H. Moench, and J. B. Thompson, Jr., "Bedrock Geologic Map of New Hampshire", Reston, VA, U.S. Geological Survey Special Map, 1:250,000, 2 sheets, 1997.

Mader, C.L., *FORTRAN BKW: A Code for Computing the Detonation Properties of Explosives*, LA-3704, Los Alamos Scientific Laboratory, Los Alamos, NM, 1967.

Martin, R., P. Boyd, A. Stroujkova, M. Leidig, J. Lewkowicz, and J. Bonner, "Anisotropy of Barre Granite in the Vicinity of NEDE," *Proc. of 2012 Monitoring Research Review: Ground-Based Nuclear Explosion Monitoring Techniques*, pp. 428–440, 2012.

Napoli, V. and D. R. Russell, "Transmission and reflection of fundamental mode *Rg* signals from atmospheric and underground explosions," *Bull. Seism. Soc. Am.*, **108**, 6, pp. 3590–3597, doi:10.1785/0120180084, 2018.

Naugolnykh, K. and L. Ostrovsky, Nonlinear Wave Processes in Acoustics, Cambridge Univ. Press, Cambridge, 1998.

Naylor, R.S., "Age and origin of the Oliverian domes, central-western New Hampshire," *Geological Society of America Bulletin*, **80**, pp. 405–427, 1969.

Patton, H. and S. Taylor, "Effects of shock-induced tensile failure on mb-Ms discrimination: Contrasts between historic nuclear explosions and the North Korean test of 9 October 2006," *Geophys. Res. Lett.*, **35**, L14301, doi:10.1029/2008GL034211, 2008.

Patton, H. J. and S. R. Taylor, "The apparent explosion moment: Inferences of volumetric moment due to source medium damage by underground explosions," *J. Geoph. Res.*, **116**, B03310, doi 10.1029/2010JB007937, 2011.

Perret, W.R. and R.C. Bass, *Free-field ground motion induced by underground explosions*, SAND-74-0252, Sandia National Labs, Albuquerque, NM, Web. doi:10.2172/4227056, 1975.

Russell, D.R., "Development of a time-domain, variable-period surface wave magnitude measurement procedure for application at regional and teleseismic distances. Part I – Theory," *Bull. Seism. Soc. Am.*, **96**, pp. 665–677, 2006.

Sammis, C.G., "Effect of the burn rate on the spatial extent of fracture damage in an underground explosion," *Proceedings of the 2011 Monitoring Research Review on Nuclear Monitoring Technologies*, Tucson AZ, pp. 572–577, 2011.

Snell, C., D. Oltmans, and E. Leahy, *Prediction of airblast overpressures from underground explosions*, EERO Technical Report No. 7, National Technical Information Service, Springfield, VA, 32 pp, 1971.

Stroujkova, A., J. Bonner, M. Leidig, P. Boyd, and R. Martin, "Shear Waves from Explosions in Granite Revisited: Lessons Learned from the New England Damage Experiment," *Bull. Seism. Soc. Amer.*, **102**, pp. 1913–1926, doi:10.1785/0120110204, 2012.

Stroujkova, A., M. Leidig, and J. Bonner, "Effect of the Detonation Velocity of Explosives on Seismic Radiation," *Bull. Seism. Soc. Am.* **105**, pp. 2367–2378, doi:10.1785/0120140115, 2015a.

Stroujkova, A., "Effect of Explosion Gaseous Products on Seismic Coupling for Underground Chemical Explosions," *Bull. Seism. Soc. Amer.*, **105**, pp. 2367–2378, doi:10.1785/0120140360, 2015b.

Stroujkova, A., M. Carnevale, and O. Vorobiev, "Cavity Radius Scaling for Underground Explosions in Hard Rock," *Bull. Seismol. Soc. Am.* **106**, doi: 10.1785/0120160122, 2016.

Stroujkova, A., "Rock Damage and Seismic Radiation: A Case Study of the Chemical Explosions in New Hampshire," *Bull. Seism. Soc. Am.*, **108**, 6, pp. 3598–3611, doi:10.1785/0120180117, 2018a.

Stroujkova, A, "Relative Moment Tensor Inversion with Application to Shallow Explosions and Earthquakes," *Bull. Seism. Soc. Amer.*, **108**, 5A, pp. 2724–2738, doi:10.1785/0120180082, 2018b.

Vortman, L. J., *Close-in airblast from a Nuclear Detonation in Basalt, Project DANNY BOY*, POR-1810, Sandia Laboratories, Albuquerque, New Mexico, 1962.

Vortman, L. J., "Close-in air blast from underground explosions," in *Proc. Eng. with Nuclear Expl.*, January 14-16, 1970, Las Vegas, NV, pp. 1508–1543, 1970.

LIST OF SYMBOLS, ABBREVIATIONS, AND ACRONYMS

AFRL	Air Force Research Laboratory
AFSPC	Air Force Space Command
AFWA	Air Force Weather Agency
ATV	Acoustic Televiewer
ANFO	Ammonium Nitrate and Fuel Oil
BKW	Becker-Kistiakowski-Wilson
CLVD	Compensated Linear Vector Dipole
COMP B	Composition B
EOS	Equation of State
IRIS	Incorporated Research Institutions for Seismology
MT	Moment Tensor
OTV	Optical Televiewer
PASSCAL	Program for the Array Seismic Studies of the Continental Lithosphere
RMTI	Relative Moment Tensor Inversion
SNR	Signal-to-Noise Ratio
TNT	Trinitrotoluene
VOD	Velocity of Detonation

DISTRIBUTION LIST

DTIC/OCP
8725 John J. Kingman Rd, Suite 0944
Ft Belvoir, VA 22060-6218 1 cy

AFRL/RVIL
Kirtland AFB, NM 87117-5776 1 cy

Official Record Copy
AFRL/RVB/Dr. Frederick Schult 1 cy

This page is intentionally left blank.